Seismic Response Analysis of Submerged Slopes using Coupled SPH-DEM Scheme

Saman Farzi Sizkow[*], Usama El Shamy[†]

December 20, 2021

Abstract

In this study, the seismic response of submerged slopes is evaluated using a coupled smoothed particle hydrodynamics (SPH) - discrete element method (DEM) technique. In this method, DEM particles represent the soil grains and the fluid domain is idealized using SPH. The interaction forces between the two phases are estimated based on well-established semi-empirical equations. The submerged slope was created utilizing the coupled scheme and subjected to a variety of base excitations with various amplitudes and frequencies. The results suggest that the stronger input motion generally induces larger displacements and shear strains. Additionally, the frequency of the input motion can also have a significant impact on the level of deformation the system experiences. It was observed that the soil strength and stiffness can severely

[*]Graduate Research Assistant, Civil and Environmental Engineering Dept., Southern Methodist University, PO Box 750340, Dallas, TX 75275, E-mail: sfarzisizkow@smu.edu

[†]Associate Professor, Civil and Environmental Engineering Dept., Southern Methodist University, PO Box 750340, Dallas, TX 75275, E-mail: uelshamy@lyle.smu.edu (Corresponding author)

degrade due to pore pressure buildup, leading to excessive lateral deformations at input motion frequencies considerably lower than the initial fundamental frequency of the deposit. Contrary to the level parts of the model near the slope toe and crest, soil dilation close to the slope surface leads to a drop in the excess pore pressure and a temporary regain in soil strength and stiffness reflected by sharp acceleration spikes and asymmetrical shear stress-strain loops.

1 INTRODUCTION

Earthquake-induced damages on slopes and nearby structures can be catastrophic. Slope failure is occasionally accompanied by extensive deformations and landslides that potentially lead to substantial financial and life losses. Seismic slope instability can be broadly categorized into inertial instability and weakening instability. In inertial instability, the soil maintains its shear strength during seismic loading and shear strain is produced due to development of dynamic shear stresses that temporarily exceed the available soil strength. A variety of techniques which are typically suited for dry soils can be used to evaluate this type of slope instability, including pseudo-static analysis, sliding block techniques (Newmark-type techniques), and stress-deformation approaches. Weakening instability occurs when the earthquake results in a significant loss of soil strength to a point where it cannot sustain the dynamic or even static shear stresses. This type of instability can be divided into the two main groups of flow failure and deformation failure (Kramer, 1996). In flow failure, the soil strength drops below the static shear stresses leading to sudden large deformations. Deformation failure corresponds to a situation where the soil shearing resistance is weakened enough to be surpassed by the dynamic shear stresses in short time intervals, resulting in gradual accumulation of permanent deformation. One of the main sources of soil strength degradation is the generation of pore pressure during seismic excitation. Due to their complex nature, centrifuge testing and numerical modeling are commonly used for the seismic response analysis of saturated slopes.

Centrifuge modeling has been frequently used to study the complex response of various geotechnical systems and also as a validation tool for numerical simulations. While field data and case histories provide useful information, centrifuge testing enables the researchers to acquire deeper insight into the mechanisms leading to the observations. In this approach, a small-scale version of the prototype is constructed for use in the lab experiments. In order to have a similar state of stresses within the model and the original system, the g-level is artificially increased by applying a centrifugal force to the model. In addition, further adjustments are made, according to the scaling laws, to different model parameters such as fluid viscosity, input motion amplitude, input motion frequency and duration of excitation. Many researchers adopted this technique to study different phenomena concerning the seismic response of saturated slopes, such as lateral spreading and flow failure induced by void redistribution (e.g. Liu and Qiao (1984); Elgamal et al. (1989); Dobry and Liu (1992); Kokusho (1999); Olson and Stark (2003); Kamai and Boulanger (2010); Boulanger et al. (2014); Lu et al. (2019)).

A range of numerical techniques are available for stability analysis of saturated slopes. Mesh-based continuum methods, such as the finite element method (FEM) and the finite difference method (FDM), generally use sophisticated constitutive models along with relatively large number of parameters to be able to capture complicated stress-strain soil behavior (e.g. Wakai and Ugai (2004); Malvick et al. (2006); Elgamal et al. (2009); Kamai and Boulanger (2013); Madabhushi et al. (2018); Boulanger et al. (2014); Boulanger and Montgomery (2016); Gu et al. (2021)). The material point method (MPM) is an Eulerian-Lagrangian technique, in which the material points, representing the continuum media, move within a fixed background mesh. This method was developed as an extension of FEM designed for large deformation problems such as landslides. However, this method still suffers from the need for a complex constitutive model to replicate the complicated soil response patterns. There have been some studies utilizing this method to simulate liquefaction-induced slope instability (e.g. Cuomo et al. (2019); Soga et al. (2016)). The smoothed particle hydrodynamics (SPH) is a meshless technique based on discretization of the computational domain (fluid or solid) into individual particles and smoothing of different quantities using a kernel function. This method is also suitable for large strain simulations thanks to its Lagrangian framework. SPH was employed to analyze the slope response in the presence of pore water pressure (e.g. Chen and Qiu (2014); Zhang et al. (2019)).

The discrete element method (DEM) is also a meshless technique developed by Cundall and Strack (1979). In this method, the soil is simulated as a collection of rigid particles (spherical or irregular-shaped), interacting with each other at the contact points. DEM provides the most realistic representation of granular soil and, without the need for a complicated constitutive model or many simplifying assumption, is able to automatically capture the micro-scale mechanisms and inherently account for soil non-linearity, soil non-homogeneity, and possibility of large deformations. This method has been utilized in various areas of geotechnical engineering (e.g. Zamani and El Shamy (2011); Dobry and NG (1992); Thornton (2000); Radjaï and Dubois (2011); Sizkow and El Shamy (2021b)). Considering the advantages of DEM in simulating granular materials, several coupled algorithms incorporating different computational fluid dynamics (CFD) methods have been constructed to account for the presence of pore water between DEM particles. However, apart from few instances where different coupled CFD-DEM methods were used to study lateral spreading and shear localization in mildly sloping deposits (e.g., El Shamy et al. (2010); El Shamy and Abdelhamid (2017); Sizkow and El Shamy (2021c); El Shamy and Sizkow (2021b)), to the best of authors knowledge, previous applications of DEM to slope stability problems involve rock materials or dry soil and no studies have been presented to model submerged slopes based on DEM.

Two of the most common fluid coupling schemes involving DEM are continuum-discrete methods (e.g., El Shamy and Zeghal (2005); Gu et al. (2020); Zou et al. (2020)), and pore-scale techniques (e.g., Zhu et al. (1999); El Shamy and Abdelhamid (2014)). The first category employs a fixed coarse grid mesh and a continuum description of the fluid. This type of space discretization significantly reduces the simulation time, however at the same time, poses obvious limitations with respect to problem geometry and boundary conditions. The second group of coupled techniques model fluid at the pore scale. Although these methods benefit from a higher degree of accuracy, the computational costs are immense for practical applications with realistic particle sizes on typical desktop computers.

As an intermediate approach in terms of efficiency and accuracy, a coupled SPH-DEM scheme has been proposed in recent years. In this method, the behavior of the fluid-particle mixture is simulated using the average forms of Navier–Stokes equations and the interphase interaction forces are calculated based on well-established semi-empirical formulas. Numerous instances of application of this technique to a variety of chemistry, physics and engineering topics can be found in the recent literature (e.g., Sun et al. (2013); Markauskas et al. (2018); Cleary (2015); Wu et al. (2016); El Shamy and Sizkow (2021a)). Compared to the fully continuum-based methods, apart from the inherent benefits of DEM, this coupled scheme is capable of successfully capturing complicated phenomena related to seismic response of saturated soils such as pore water pressure generation, degradation of soil strength and stiffness, deamplification of input motion in liquefied layers, and regain in soil strength due to dilative soil behavior without the need for a sophisticated constitutive model or many simplifying assumptions (El Shamy and Sizkow, 2021a; Sizkow and El Shamy, 2021c; El Shamy and Sizkow, 2021b). The familiar trends captured by the coupled SPH-DEM method are, unlike the continuum-based techniques, direct results of micromechanical mechanisms such as the mutual interaction between the soil particles and fluid, local volumetric strain due to rearrangement of soil particles, and changes in the average number of contacts between soil particles. In addition, due to being fully particle-based, it is very suitable for simulating large deformations, which is vital in effective modeling of slope failure. Compared to the continuum-discrete techniques (in which the fluid domain is discretized into large fixed cells), it can handle much more complicated model geometries, as the SPH particles can be placed in different configurations to fit the model requirements. In addition, the presence of free-field conditions on the sides of the model requires movable boundary conditions that pose a big challenge for the fixed-mesh techniques. Finally, compared to the pore-scale methods such as LBM-DEM, it is computationally far less demanding while displaying comparable accuracy (Sizkow and El Shamy, 2021a). The main drawback of this technique is the fact that the fluid is assumed to be weakly compressible, which can be compensated for by using a large enough numerical speed of sound that limits the density fluctuations to very small values.

The authors previously showed the capabilities of this technique in simulating several geotechnical problems (El Shamy and Sizkow, 2021a; Sizkow and El Shamy, 2021c; El Shamy and Sizkow, 2021b). In this study, the aforementioned SPH-DEM scheme was extended to analyze the seismic response of submerged slopes. A novel approach is presented herein for handling cases with free-field boundary conditions. The ability of the proposed scheme in simulating large-scale geotechnical systems with more complicated geometries is demonstrated. In this study, the soil was represented as an assembly of rigid spherical bodies with rolling friction installed between them to compensate for their idealized shape and the fluid domain was created using SPH particles. Due to similarity of the model setup to plane-strain problems, only a thin slice of the model with periodic boundaries at the front and back faces was considered for the simulations to save computational time. Furthermore, the free-field conditions were directly applied to the lateral sides of the model to reduce the refection of the propagating waves. Input motions with different combinations of frequencies and amplitudes were applied to the submerged slope and the responses of the model to different base excitations were compared to discover the effects of input motion amplitude and frequency. In addition, various parameters contributing to the loss of soil strength and slope deformation such as volumetric strain, excess pore pressure, vertical drag force and coordination number are investigated.

2 COUPLED SPH-DEM SCHEME

In the proposed coupled scheme, SPH was employed to solve the equations of fluid motion. In SPH, the fluid domain is replaced by a set of discrete particles holding local fluid properties such as density and pressure (Monaghan, 1992). The average forms of continuity and momentum equations were discretized through interpolation of various quantities over the influence domain of any given particle. The equation of state for weakly compressible fluid was utilized to evaluate the fluid pressure based on the local density. In addition, negligible density fluctuations were ensured by setting the numerical speed of sound to a proper value. Soil particles were modeled by rigid spherical particles in DEM with rolling friction between them to limit their unrealistic relative rotations. The coupling forces between the soil and fluid were also quantified using well-established semi-empirical relations, in which the interactions are calculated based on the local porosity and relative velocities between the two phases. The DEM cycles were performed using the PFC3D software (Itasca, 2018) and the SPH part of the coupled scheme was implemented using a user-written Cython code and linked to the PFC3D environment. The fluid and solid phase equations were solved using explicit time integration schemes. A constant value was selected for the DEM timestep. The SPH timestep was assumed to be N times the DEM timestep, where N is an integer. This means that N DEM computation cycles should be performed per one SPH cycle. The first step in a single SPH-DEM computational loop is to calculate the fluid particle properties such as porosity and pressure. The interaction forces are next obtained based on the latest positions and velocities of DEM particles, and the interpolated porosities at their locations. Then the SPH particle densities, velocities and positions are updated according to the variation rates of density and velocity computed from their pressure, superficial density and the coupling forces. Finally, the interaction forces are applied to the solid particles and N DEM cycles are performed to get the updated particle positions and velocities. The new positions and velocities are then sent as inputs to the SPH algorithm and the next loop begins. A brief description of the model components are provided in the following sections.

Due to some major issues, it was not possible to conduct a one-to-one comparison with published centrifuge studies on the response of submerged slopes. Some of these difficulties were: 1) The sand used in centrifuge tests is typically medium to fine sand. Replicating such sizes in DEM would require a massive number of particles that would render the simulation time impractical. 2) The model setup in the centrifuge tests requires the lateral boundaries to be placed far away from the slope in order to represent the free-field conditions. Such large models would need a huge number of DEM particles to simulate and the computational costs would be immense. 3) In most centrifuge studies, the dynamic soil properties are not fully described which makes it very difficult to create a relatively accurate numerical model of the real soil deposit. In view of these difficulties, a building block approach was adopted by the authors to validate the proposed coupled SPH-DEM model (Sizkow and El Shamy, 2021c; El Shamy and Sizkow, 2021a). The main coupling parameters between the fluid and particles in this model stem from porosity calculation, averaged solid particle velocities and the resulting drag force. Therefore, a simulation was performed to examine the ability of the model to correctly predict the drag force on a few settling particles in a fluid column (El Shamy and Sizkow, 2021a). Since this system has a diluted concentration of particles, it presents an extreme in computing porosity and associated drag forces. It also includes the challenge of large solid particle velocities. Additionally, another extreme situation in which flow in a dense stagnant arrangement of a porous medium was considered to examine the ability of the fluid code to accurately predict fluid velocities in such a dense packing (Sizkow and El Shamy, 2021c). More details on the coupled scheme, its implementation and various validation cases can be found in Sizkow and El Shamy (2021c) and El Shamy and Sizkow (2021a).

2.1 Fluid phase

The motion of solid-fluid mixture is described by the averaged forms of Navier-Stokes equations (Anderson and Jackson, 1967):

$$\frac{\partial(n\rho_f)}{\partial t} + \nabla.(n\rho_f \mathbf{u}) = 0 \quad (1)$$

$$\frac{\partial(n\rho_f \mathbf{u})}{\partial t} + \nabla.(n\rho_f \mathbf{u}\mathbf{u}) = -\nabla P + \nabla.\boldsymbol{\tau} + n\rho_f \mathbf{g} - \mathbf{f}^{\mathbf{int}} \quad (2)$$

in which P is the fluid pressure, n is the porosity, $\boldsymbol{\tau}$ is the viscous stress tensor, $\mathbf{g}$ is the gravitational acceleration vector, ρ_f is the fluid density, $\mathbf{f}^{\mathbf{int}}$ is the fluid-particle interaction force and $\mathbf{u}$ is the fluid velocity.

In SPH, the fluid domain is discretized into lumped masses carrying local fluid properties, and different quantities are interpolated using a kernel function (W). The Wendland kernel function is employed in this study (Dehnen and Aly, 2012).

Eqs. 1 and 2 can be rewritten in discrete form using SPH particle summation as:

$$\frac{d(n_i\rho_i)}{dt} = \sum_j m_j \mathbf{u_{ij}}.\nabla_i W(\left|\mathbf{r_{ij}}\right|,h) \tag{3}$$

$$\frac{d\mathbf{u_i}}{dt} = -\sum_j m_j [\frac{P_i}{(n_i\rho_i)^2} + \frac{P_j}{(n_j\rho_j)^2} + R_{ij}(\frac{W(\left|\mathbf{r_{ij}}\right|,h)}{W(\Delta p,h)})^4]\nabla_i W(\left|\mathbf{r_{ij}}\right|,h) + \mathbf{\Pi}_{ij} + \frac{\mathbf{f^{int}}}{m_i} + \mathbf{g} \tag{4}$$

where $\mathbf{u_{ij}}$ is the relative velocity vector, P_i is the fluid pressure, R_{ij} is the tensile instability term and $\mathbf{\Pi}_{ij}$ is the viscosity term (Morris et al., 1997; Monaghan, 2000).

The fluid pressure is estimated using the equation of state for weakly compressible fluid. In order to model an almost incompressible fluid, the numerical speed of sound must be selected sufficiently large to limit the magnitude of density fluctuations to very small values.

Two main types of boundary conditions are employed for the fluid in this study, namely periodic boundaries and no-slip no-penetration boundaries. Periodic boundaries represent a condition where the domain is repeated on both sides. Therefore, if a fluid particle exits the domain through one side, another particle with the same properties and velocity enters the domain from the opposite side. In addition, since the two sides are assumed to be adjacent, the spherical domain of each SPH particle near such boundaries will be completed by the particles on the other side. The method proposed by Adami et al. (2012) is used to implement no-slip no-penetration boundaries.

2.2 Solid phase

In the linear contact model, the interaction of DEM particles is described by a set of normal and shear springs and dashpots. The relative particle movements produce normal and shear elastic forces in the springs, and the viscous behavior is provided by the dashpots. In granular systems, the energy dissipates through various micro-mechanical processes, such as contact adhesion, surface roughness and particle non-sphericity (Itasca, 2018). When the soil grains are idealized as spherical DEM particles, the effects of particle shape on the energy loss during relative rotation of particles, can be compensated for by addition of rolling friction between particles (Iwashita and Oda, 1998; Oda et al., 1982). In this study, the rolling resistance contact model is utilized which is similar to the linear contact model, but with the difference that the relative rotation of particles generates a moment that resists their motion and acts as a energy dissipation mechanism (Itasca, 2018).

2.3 Fluid-solid interaction

The force applied by the fluid on the DEM particle a can be resolved into the drag force ($\mathbf{F_a^D}$) and pressure gradient force ($\mathbf{F_a^P}$) (Markauskas et al., 2017):

$$\mathbf{F_a^{int}} = \mathbf{F_a^D} + \mathbf{F_a^P} \tag{5}$$

The semi-empirical relation proposed by Ergun (1952) is used to estimate the fluid drag force based on the local porosity and the relative velocity between the two phases:

$$\mathbf{F_a^D} = \frac{\beta V_a}{1-n_a}(\mathbf{\bar{u}_a} - \mathbf{u_a}) \tag{6}$$

where $\mathbf{\bar{u}_a}$ is the average local fluid velocity, $\mathbf{u_a}$ is the solid particle velocity, V_a is the solid particle volume, β is the interphase momentum exchange coefficient and n_a is the average local porosity. β can be obtained from two separate relations based on the local porosity (Ergun, 1952):

$$\beta = \begin{cases} 150\frac{(1-n_a)^2}{n_a}\frac{\mu}{d_a^2} + 1.75(1-n_a)\frac{\rho}{d_a}\left|\mathbf{\bar{u}_a} - \mathbf{u_a}\right| & n_a \leq 0.8 \\ 0.75C_d\frac{n_a(1-n_a)}{d_a}\rho\left|\mathbf{\bar{u}_a} - \mathbf{u_a}\right| n_a^{-2.65} & n_a > 0.8 \end{cases} \tag{7}$$

in which μ is the fluid dynamic viscosity, d_a is the solid particle diameter and C_d is the drag coefficient (Ergun, 1952).

If the pressure gradient is only due to interaction between the solid particles and the fluid, the total fluid force can be rewritten as (Markauskas et al., 2017):

$$\mathbf{F_a^{int}} = \mathbf{F_a^D} + \mathbf{F_a^P} = \frac{\mathbf{F_a^D}}{n_a} - V_a\rho_f\mathbf{g} \tag{8}$$

The fluid particle i will also receive reaction forces from all DEM particles within its support domain. The total force is given by:

$$\mathbf{f_i^{int}} = -\frac{m_i}{\rho_i}\sum_a \frac{W(|\mathbf{r_{ai}}|, h)}{\sum_j \frac{m_j}{\rho_j} W(|\mathbf{r_{aj}}|, h)}\mathbf{F_a^{int}} \tag{9}$$

For the kernel function used in this study, the influence domain of each particle is a sphere with a radius of 2h (h is the smoothing length). A schematic view of the SPH-DEM model is presented in Fig. 1.

3 Model Description

A submerged slope was created using the proposed SPH-DEM approach. In order to downscale the model to a manageable size, a high gravitational field of 50g was employed and the model dimensions and input parameters were adjusted according to centrifuge scaling laws (Iai et al., 2005). The results presented in this study are in prototype units unless otherwise specified. Due to similarity of the model setup to a plane-strain problem, only a thin slice of the slope (with a thickness of 1.2 m) was modeled, and periodic boundary condition was applied to the front and back faces of the model. These boundaries represent a condition where the model is infinitely extended on both sides. The model had heights of 7 m and 4 m at the slope crest and toe, respectively. The slope had an angle of approximately 22 degrees and a width of 7.5 m. The total width of the model was selected to be 52.5 m to enable the implementation of free field conditions as explained later in this section. To create the soil deposit, first the number of required DEM particles with sizes ranging from 1.5 mm to 2.5 mm was calculated based on the desired porosity and the model dimensions. These particles were then generated in a larger space and released to settle under gravity to create a level deposit with a height of around 7 m (height of the slope crest). In the next step, a portion of the deposit was removed to create a slope with the targeted angle and width. Finally, the model was allowed to reach equilibrium. The porosity and saturated unit weight of the deposit were determined to be around 0.43 and 19 kN/m^3, respectively. In addition, the soil friction angle was found to be around 30 degrees using a numerical drained triaxial test on a sample with the same properties and packing density. The static factor of safety against slope failure can be calculated based on the slope geometry and the soil properties. GeoStudio 2021 was used for the static stability analysis and the safety factor was found to be approximately 1.45. Since spherical particles were used in the study, rolling friction was added between them to limit their excessive relative rotations and account for the irregular shape of the real soil grains.

A fluid domain with a height of 7.5 m was created using SPH particles to fully cover the submerged slope. Periodic boundary conditions were also applied for the front and back faces of the fluid domain. The initial spacing and smoothing length (h) of the SPH particles were 4 mm and 6 mm, respectively. These values were chosen carefully to produce a smooth porosity field without losing much information (Sizkow and El Shamy, 2021c). The bottom of the deposit was modeled by a rigid wall in DEM and by a no-slip, no-penetration boundary in SPH to simulate a bedrock. The input motions were later applied to the models through this base wall. In addition, due to the use of SPH, a free surface boundary condition is automatically applied at the top of the model.

The lateral boundaries of the model needed special treatment to prevent the reflection of the propagating waves. The authors previously developed a free-field boundary condition for dry geotechnical systems in DEM (Sizkow and El Shamy, 2021b). However, due to various complications caused by the pore pressure buildup, a different approach was chosen for the saturated deposits. This approach is based on the fact that the free-field condition can be practically assumed at points far enough from the surface structure. Therefore, if the lateral sides of the model are placed sufficiently far from the slope, the quantities measured within the free-field can be directly applied to them without causing much reflection. The lateral boundaries were implemented in several steps: (1) Two periodic saturated soil columns with the same properties as the main model (porosity, particle size, fluid viscosity and so on) and heights equal to the heights of the slope crest and toe (7 m and 4 m, respectively) were first created. (2) These free-field columns were then subjected to the same input motion that was going to be later introduced to the main model and the time histories of different average quantities were recorded for both phases at different heights such as particle velocities, fluid velocities, fluid density and pressure. This step was done for each input motion separately. (3) Two thin boundary layers were selected at both sides of the main model and the fluid and soil particles within them were identified at different heights. (4) During the main simulation, the previously recorded quantities were directly applied to the soil and fluid particles inside these thin boundary layers at the corresponding heights in sync with the base excitation. A schematic of the main model along with the steps for implementing the lateral boundaries are presented in Fig. 2. This method is only effective if the conditions at the lateral sides of the model are close to those of free-field. Therefore, a sensitivity analysis was needed in order to find the proper margins for both sides of the model. To this end, the model was extended on both sides in several steps, and simulations with the same input motion were performed. The results revealed that when the lateral boundaries were more than 19 m away from the slope crest and toe, the response remained almost unaffected. The margin for the final model was selected to be 22.5 m for both sides which is 3 times the width of the slope.

A 3D view of the submerged slope is shown in Fig. 3. The centrifuge scaling laws dictate that the model dimensions must be reduced by a factor of 50 compared to the prototype while the fluid viscosity must be increased by the same factor (Iai et al., 2005). In addition, to compensate for relatively large particle sizes used in this study, a high prototype fluid viscosity of 0.02 Pa.s was used. Based on the model properties and using the Kozeny-Carmen equation (Carman, 1937) the initial permeability of the deposit is approximately 3 mm/s which is close to that of coarse sand. A summary of various parameters used in the performed simulations is presented in Table 1.

Sinusoidal input accelerations with maximum amplitudes of 0.001g, 0.1g and 0.25g and various frequencies were introduced into the model through the base rock. The amplitude of the input accelerations linearly increases from zero to its peak in the first 3 seconds. Then it remains at its maximum level for the next 4 seconds, and during the last second of loading (from 7 s to 8 s) its amplitude linearly reduces to zero. Based on the scaling laws (Iai et al., 2005), the input frequencies and amplitudes in the model must be 50 times higher than the prototype while the shaking duration must be reduced by a factor of 50. Several parameters at different locations were monitored throughout the model during the base excitation, including average soil and fluid particle velocities, average excess pore pressure, packing porosity, average drag force, stress and strain tensors and coordination number.

The maximum input accelerations of 0.1g and 0.25g were selected as moderate and severe seismic events, respectively. The simulations with maximum acceleration of 0.001g, due to low level of strains induced during them, were used to determine different dynamic properties of the deposit such as fundamental frequency, shear wave velocity and low strain shear modulus. Table 2 shows the dynamic properties derived from these simulations. In addition, the free-field amplification factors at the crest side (height of 7 m) for various input motion frequencies are presented in Table 3. The results show that the maximum amplification of the input motion occurred at the frequency of 4 Hz which is close to the fundamental frequency of the slope crest (4.1 Hz). The amplification factors were also compared with the analytical expression for one dimensional wave propagation in elastic solids (Kramer, 1996). A relatively close agreement can be observed between the results. Note that in the analytical solution, the damping coefficient of the soil was assumed to be 0.05.

4 Response of Submerged Slope

This section presents the results of the main simulations with the maximum input acceleration amplitudes of 0.1g and 0.25g, and frequencies of 1 Hz and 3 Hz. For the input motion of 0.1g-3 Hz, although pore pressure buildup and degradation of soil stiffness and strength were observed, its impact was not so devastating that it would complicate the analysis of the response. Therefore, this simulation is studied in depth and a summary of the results for other simulations are provided at the end.

Fig. 4 shows the contours of excess pore pressure ratio at different time instants during the 0.1g-3 Hz simulation. The value of 1 is generally considered as an indication of the onset of liquefaction where the effective stress is counterbalanced by the excess pore pressure. Gradual development of pore pressure inside the deposit can be seen from 3 s to 7 s. At 7 s, values close to one are reached at both sides of the slope near the ground surface signifying liquefaction of these layers, while deeper locations displayed much lower values. The situation in the middle directly below the slope, however, quite differs from the sides and the excess pore pressure is substantially lower in this area. It will be shown later that this is due to the dilative behavior of soil in that region. Dissipation of pore pressure can also be observed after the end of loading at 9 s and 10 s.

Generation of pore pressure is a direct result of changes in pore space volumes. The contours of volumetric strain at various moments throughout the 0.1g-3 Hz simulation are presented in Fig. 5. Large negative volumetric strains are visible after the first 7 seconds at the side locations near the surface, suggesting contraction of pore spaces at these points that led to high pore pressure buildup. Deeper locations evidently experienced less volumetric strain and, consequently, less pore pressure. For the region below the slope, considerably smaller negative volumetric strains or even positive values denoting dilation, were observed that explains the lower pore pressure in this area.

Fig. 6 demonstrates the time histories of particle and fluid accelerations at different locations inside the deposit. At side locations close to the surface, the ground motion was initially amplified and then gradually decreased due to development of pore pressure after the first 3 seconds. Negative acceleration spikes can also be seen directly below the slope (locations 5, 10 and 11) indicating soil dilative behavior at these points (Elgamal et al., 2002). The decrease in the acceleration amplitude in the liquefied soil is due to the large drag forces arising from the excess pore pressure buildup, that separate particles from each other and lead to loss of interparticle contacts. It is also worth noting that the fluid and particle accelerations were virtually the same at various locations with a very small phase difference. This was expected due to the coupling forces between the two phases that leads to fluid phase closely following the motion of the solid phase.

The contours of vertical drag force normalized by average particle weight, and coordination number at various points in time are presented in Figures 7 and 8. According to Fig. 7, the area with a normalized value of 1, progressively expanded during the base excitation starting from the surface at both sides of the slope, implying that the entire weight of particles was carried by the fluid and hence liquefaction. As a result, the drop in acceleration amplitude was more pronounced at these points. For deep layers, this ratio is around 0.4 originating mainly from the buoyancy force. At layers directly below the slope in contrast to the sides, the drag forces are considerably smaller because of the lower excess pore pressure. As the pore pressure vanished by the end of simulation, the drag forces reduced again to the buoyancy forces. At the start of the simulation the coordination number is clearly higher than the threshold value of 4, suggesting that the model is stable under the static loads (Edwards, 1998). However, during the seismic loading, the coordination number dropped below 4 in the shallow layers, especially on the sides where it reached values as low as

2.5. This was expected due to the large excess pore pressure and associated drag forces on both sides of the slope. Immediately below the slope, coordination numbers below 4 are visible denoting instability, however, the values are larger compared to the locations at both sides. It is also worth mentioning that the coordination number in almost the entire deposit increased again to values higher than 4 needed for stability after the loading ended (at 9 s and 10 s).

Plots of cyclic shear stress-strain loops can be seen in Fig. 9. Degradation of soil strength and stiffness could be seen especially at the zones of high pore pressure. Contrary to the two sides of the slope where the stress-strain loops are symmetric, in the middle locations, much larger shear stresses were developed in one direction and the bottom part of the loops seems to be relatively flat. The reason is the dilative behavior at these points and the temporary gain in soil strength which is later examined. Large cyclic shear strains in the order of 0.25 to 0.5% developed near the surface (see locations 1, 16 and 17). Time histories of cyclic shear stress versus total shear strain are shown in Fig. 10. At the shallow depths on both sides, shear stress gradually reduced after the first few seconds of base excitation and shear strain started to accumulate. Much larger shear strains (higher than 12%) can be observed near the slope surface (locations 5, 6, 10 and 11). It can also be seen that the development of shear strain mainly occurred during intervals where the cyclic shear stress was negative (the acceleration was upslope).

Fig. 11 shows the accumulation of maximum shear strain at the selected time instants. In order to obtain these contours, first, the strain-rate tensors were recorded at a large number of points close to the slope. Then the strain tensors were computed by integrating the strain-rate tensors. Finally, the principal strains and maximum shear strains were calculated by obtaining the eigenvalues of the strain matrix. According to this figure, the slope underwent the maximum shear strain of approximately 17.8% near its surface. In addition, formation of a circular zone of high shear strain near the slope surface is obvious in this figure. The accumulation of shear strain near the slope is due to large dynamic shear stresses that briefly surpass the available soil strength and result in sliding of the particles. The contours of maximum shear stress normalized by the confining effective stress are provided in Fig. 12. The contours correspond to the time instants when the acceleration was in the upslope direction. The normalized maximum shear stress gradually increased, reaching values around 0.5 within a circular shape extending down to the slope toe. Fig. 13 demonstrates the displacement contours throughout the 0.1g-3 Hz simulation. The circular shape of the contours can again be noticed in this figure. The maximum displacement according to these contours was higher than 35 cm located close to the slope crest.

To better understand the underlying mechanisms behind some of the trends observed in the response of the submerged slope, a few loading cycles were closely inspected to discover how different quantities are correlated. Fig. 14(a) shows the location of the measurement point at which various quantities were evaluated during a short time window and presented in Fig. 14(b to e). Point 1 corresponds to a time when the velocity at the measurement point has just reached its maximum in the downslope direction and started accelerating upslope (Fig. 14(b and c)). At this instant, the excess pore pressure ratio near the slope surface is highest during the selected interval (Fig. 14(a)). Due to higher pore pressure, the soil exhibits lower strength and, therefore, the acceleration time history (Fig. 14(b)) becomes fairly flat moving toward point 2. However, at point 2, where the acceleration is still in the upslope direction, the pore pressure near the slope surface vanishes and the soil strength and stiffness are partly recovered. This leads to a small increase in the acceleration and higher inclination of the stress-strain loop after this point (Fig. 14(b and e)). Moving from point 2 to 3, where the velocity reduces in the upslope direction and the acceleration is downslope, the pore pressure is mostly negative near the slope surface and the soil strength and stiffness are relatively high. As a result, the input acceleration is almost fully transmitted from the base to the slope surface and a negative spike is formed (Fig. 14(b)). From point 3 to 4, where the maximum velocity in the downslope direction is reached, the pore pressure builds up again and the condition becomes similar to point 1. The same cycle (points 1-4) is repeated for points 4-6.

In order to investigate these cyclic oscillations in the pore pressure close to the slope surface, contours of cyclic volumetric strain during the same time interval are provided in Fig. 15. Note that the permanent part of the strain is eliminated to better elucidate the cyclic behavior. At point 1 when the velocity is maximum in the downslope direction, the cyclic volumetric strain is at its maximum negative level, indicating contraction of pore spaces and an increase in pore pressure near the slope surface. Between points 1 and 3, the acceleration is upslope, and the cyclic volumetric strain progressively shifts towards positive values, indicating dilation. During this stage, it first reaches almost zero at point 2 and then its maximum positive value at point 3. This dilative behavior leads to a decrease in pore pressure. From point 3 to point 5, where the acceleration is downslope, the trend is reversed. The cyclic volumetric strain first reduces to almost zero at point 4 and then reaches its maximum negative value at point 5, leading again to pore pressure buildup. This pattern is repeated throughout the simulation. It is also worth noting that the amplitude of the cyclic volumetric strain is much higher near the slope and the oscillations outside this area are not as significant. This periodic switching between contraction and dilation is due to effect of downslope component of the static shear stress.

As mentioned earlier, several simulations were performed on the same deposit with several amplitudes and frequencies. Some of the main responses of the submerged slope to four base excitations are reported here. The contours of maximum pore pressure ratio and total volumetric strain are provided in Fig. 16. Note that the contours of maximum pore pressure ratio do not correspond to any specific time instant, but they illustrate the maximum values during the entire simulation. According to Fig. 16(a), the pore pressure buildup is slightly lower for the input motion of 0.1g-1 Hz than 0.1g-3 Hz. Both simulations show small excess pore pressure in the middle area. The main difference is at the left side where the maximum excess pore pressure ratio is around 0.5 and 1.0 for the 0.1g-1 Hz and 0.1g-3 Hz simulations, respectively. The small pore pressure in this area for the input motion of 0.1g-1 Hz seems reasonable since the natural frequency of the free-field at the toe side is much higher than 1 Hz. These results can be confirmed by the contours of total volumetric strain in Fig. 16(b). The deposit experienced larger negative volumetric strains at the right side than its left during the 0.1g-1 Hz simulation, resulting in higher pore pressure close to the slope crest. For the input acceleration of 0.1g-3 Hz, the negative volumetric strain on both sides was considerable, leading to liquefaction of the shallow layers. For both input motions in the region below the slope, the soil displayed much less contractive behavior and even areas of dilation can be seen. For the input motions with the acceleration amplitude of 0.25g, the situation is opposite. During the 0.25g-1 Hz simulation, the excess pore pressure ratio of 1 was reached in the whole deposit while for the input motion of 0.25g-3 Hz, the zone below the slope exhibited much lower maximum values (around 0.5). This could be explained by the fact that the shear modulus significantly reduces when the model is subjected to the stronger acceleration of 0.25g and, therefore, a lower frequency compared to the input acceleration of 0.1g, will have the most destructive effects. For the 0.25g input motions, according to Fig. 16(b), significant volume reduction is evident on both sides of the slope, generating large excess pore pressure even in the deep layers. In the area below the slope, however, the volumetric strain seems to be mostly positive indicating dilation. This might seem counterintuitive because of the large excess pore pressure in this area, especially during the 0.25g-1 Hz simulation. The reason is that, although the net volumetric strain in the middle area is mostly positive, the cyclic volumetric strain, as observed in Fig. 15, leads to oscillations of pore pressure with possibly large amplitudes.

Fig. 17 shows the time histories of pore pressure ratio at four locations near the ground surface during the simulations. According to this figure, the average pore pressure progressively increased at locations 1 and 4 during the base excitation in all simulations. However, at locations 2 and 3, the average excess pore pressure seems to stop increasing after the first few seconds at a noticeably lower level compared to the side locations. In addition, much larger oscillations of pore pressure are visible at locations 2 and 3, especially during the 0.25g-1 Hz simulation where it reached values higher than 1. These observations are consistent with the results of the centrifuge study conducted by Taboada-Urtuzuastegui et al. (2002) on a submerged slope subjected to base excitations with amplitudes of 0.2g and 0.25g, and frequency of 1 Hz. They observed that at locations below the slope, the excess pore pressure ratio underwent large oscillations and only temporarily reached the value of 1. However, at the side locations, the ratio of one was reached and maintained during dynamic loading without any significant drops.

The time histories of average particle acceleration at the same four locations are provided in Fig. 18. Except for the 0.1g-1 Hz input motion, a gradual attenuation of particle acceleration is visible at the side locations (1 and 4). The most severe case corresponds to the 0.25g-1 Hz input motion at location 4, where the acceleration almost completely vanished after the first 4 seconds. At locations 2 and 3, again except for the 0.1g-1 Hz input motion, one-sided acceleration spikes due to soil dilation and a regain in soil stiffness can be observed. It is also worth noting that, contrary to the other cases in this study, the acceleration spikes occurred in the upslope direction during the 0.25g-1 Hz simulation with magnitudes much larger than the input acceleration (as high as 0.4g). Acceleration spikes due to soil dilative behavior near the slope were also reported in the centrifuge study conducted by Taboada-Urtuzuastegui et al. (2002).

Fig. 19 shows the contours of total displacement and maximum shear strain for different input motions. Note that due to the large gap between the results of simulations with maximum acceleration amplitudes of 0.1g and 0.25g, different ranges were chosen in these plots for more clarity. The maximum displacement and shear strain as well as the extent of the noticeably deformed area are higher for the input motion of 0.1g-3 Hz compared to 0.1g-1 Hz, but not by a large margin. This can be due to comparable amount of excess pore pressure generated inside the deposits and relatively close level of acceleration amplitudes near the slope for these two cases. The results, however, show substantially larger displacement and shear strains for the input motion of 0.25g-1 Hz compared to 0.25g-3 Hz. This can be explained by the higher pore pressure and inertial forces developed during the 0.25g-1 Hz simulation. In addition, the results of the 0.25g simulations, as expected, show considerably higher levels of deformation and shear strain than the 0.1g simulations.

The lateral displacement profiles at the selected locations are provided in Fig. 20. These plots were obtained by integrating the average particle velocities at different depths. According to this figure, at any given height, the lateral displacement was the highest at location 1 and the slope toe, while the slope crest experienced the lowest deformation. The maximum lateral displacement at the slope surface also corresponds to location 2 for all input motions. It is also worth mentioning that for the simulations with the input motion amplitude of 0.25g, the lateral spreading is noticeable even at deep locations and it almost linearly grows toward the slope surface. In case of the 0.1g simulations, the pattern is quite different and the lateral deformation suddenly increases within the shallow layers while it is negligible near the base. In addition, the results are consistent with the displacement contours presented in Fig. 19(a). The deposit experienced much larger lateral displacement during the 0.25g-1 Hz simulation compared to the 0.25g-3 Hz simulation (approximately 150 cm compared to 75 cm). The lateral deformations for the 0.1g-1 Hz and 0.1g-3 Hz simulations were fairly close at around 30 cm.

Fig. 21 shows the deformed shapes of the slope at the end of simulations. The deposit was colored in brown and black vertical stripes to better visualize particle movements. For the 0.1g-1 Hz and 0.1g-3 Hz simulations, small ground settlement can be detected at the crest side. The stripes are also slightly inclined downslope near the slope surface but the overall shape of the slope is not significantly changed. The model experienced considerably larger settlement behind the crest during the 0.25g-3 Hz simulation. In addition, lateral spreading is more pronounced compared to the 0.1g simulations, even at deep locations. The largest lateral spreading and ground settlement occurred during 0.25g-1 Hz simulation and the slope became completely deformed by the end of simulation. The ground upheaval is also visible near the slope toe.

5 Conclusions

A three-dimensional Lagrangian-Lagrangian coupled scheme is presented herein to study the response of submerged slopes to seismic base excitations. In this approach, the soil is idealized by a collection of spherical DEM particles with rolling friction between them to approximate the effect of irregularly shaped particles, and the fluid phase is simulated using SPH, by lumping the domain into discrete particles. The fluid motion is described by average forms of Navier-Stokes equations, and well-known semi-empirical relations are employed to evaluate the interaction forces between the two phases. A combination of different amplitudes and frequencies were chosen for the input motions and their impact on the response of the model were investigated. The main conclusions of this study can be summarized as follows: (1) As expected, the stronger acceleration amplitude resulted in more deformations. (2) The input motion frequency was also a governing factor in the severity of the outcome. (3) Liquefaction was marked by several response mechanisms, such as pore pressure buildup, vertical drag forces separating soil particles, low coordination numbers, and degradation of soil strength and stiffness especially in the shallow layers. (4) Dilative soil behavior close to the slope surface resulted in less pore pressure ratio compared to the level parts of the slope at the crest and toe. (5) The expansion of pore spaces near the slope surface led to a noticeable drop in the excess pore pressure and a temporary gain in soil strength and stiffness reflected by sharp acceleration spikes and asymmetrical shear stress-strain loops. (6) The shift in the natural frequency of the deposit during shaking as a result of pore pressure buildup and subsequent strength degradation, could lead to excessive lateral deformation.

The presented coupled framework is capable of successfully capturing complicated phenomena related to seismic response of saturated soils such as pore water pressure generation, degradation of soil strength and stiffness, deamplification of input motion in liquefied layers, and regain in soil strength due to dilative soil behavior without the need for a sophisticated constitutive model or many simplifying assumptions. The presented coupled SPH-DEM model appears to be a promising tool for scenario-based response analysis of geotechnical systems with far less computational demands compared to pore-scale models of the interstitial fluid.

DATA AVAILABILITY

Some or all data, models, or code generated or used during the study are available from the corresponding author by request.

Acknowledgement

This research was partially supported by the US Army Corps of Engineers Engineer Research and Development Center, grant number W9132V-13-C-0004 and the National Science Foundation award number CMMI-1728612. These supports are gratefully acknowledged.

References

Adami, S., Hu, X., and Adams, N. (2012). "A generalized wall boundary condition for smoothed particle hydrodynamics." *Journal of Computational Physics*, 231(21), 7057–7075.

Anderson, T. and Jackson, R. (1967). "Fluid mechanical description of fluidized beds. equations of motion." *Industrial & Engineering Chemistry Fundamentals*, 6(4), 527–539.

Boulanger, R., Kamai, R., and Ziotopoulou, K. (2014). "Liquefaction induced strength loss and deformation: simulation and design." *Bulletin of Earthquake Engineering*, 12(3), 1107–1128.

Boulanger, R. and Montgomery, J. (2016). "Nonlinear deformation analyses of an embankment dam on a spatially variable liquefiable deposit." *Soil Dynamics and Earthquake Engineering*, 91, 222–233.

Carman, P. (1937). "Fluid flow through granular beds." *Trans. Inst. Chem. Eng.*, 15, 150–166.

Chen, W. and Qiu, T. (2014). "Simulation of earthquake-induced slope deformation using sph method." *International Journal for Numerical and Analytical Methods in Geomechanics*, 38(3), 297–330.

Cleary, P. (2015). "Prediction of coupled particle and fluid flows using DEM and SPH." *Minerals Engineering*, 73, 85–99.

Cundall, P. and Strack, O. (1979). "A discrete numerical model for granular assemblies." *geotechnique*, 29(1), 47–65.

Cuomo, S., Ghasemi, P., Martinelli, M., and Calvello, M. (2019). "Simulation of liquefaction and retrogressive slope failure in loose coarse-grained material." *International Journal of Geomechanics*, 19(10), 04019116.

Dehnen, W. and Aly, H. (2012). "Improving convergence in smoothed particle hydrodynamics simulations without pairing instability." *Monthly Notices of the Royal Astronomical Society*, 425(2), 1068–1082.

Dobry, R. and Liu, L. (1992). "Centrifuge modeling of soil liquefaction." *Proc., 10th World Conf. on Earthquake Engineering*, 6801–6809.

Dobry, R. and NG, T. (1992). "Discrete modelling of stress-strain behaviour of granular media at small and large strains." *Engineering computations*.

Edwards, S. (1998). "The equations of stress in a granular material." *Physica A: Statistical Mechanics and its Applications*, 249(1-4), 226–231.

El Shamy, U. and Abdelhamid, Y. (2014). "Modeling granular soils liquefaction using coupled lattice Boltzmann method and discrete element method." *Soil Dynamics and Earthquake Engineering*, 67, 119–132.

El Shamy, U. and Abdelhamid, Y. (2017). "Some aspects of the impact of multidirectional shaking on liquefaction of level and sloping granular deposits." *Journal of Engineering Mechanics*, 143(1), C4016003.

El Shamy, U. and Sizkow, S. (2021a). "Coupled smoothed particle hydrodynamics-discrete element method simulations of soil liquefaction and its mitigation using gravel drains." *Soil Dynamics and Earthquake Engineering*, 140, 106460.

El Shamy, U. and Sizkow, S. (2021b). "Coupled SPH-DEM simulations of liquefaction-induced flow failure." *Soil Dynamics and Earthquake Engineering*, 144, 106683.

El Shamy, U. and Zeghal, M. (2005). "Coupled continuum-discrete model for saturated granular soils." *Journal of engineering mechanics*, 131(4), 413–426.

El Shamy, U., Zeghal, M., Dobry, R., Thevanayagam, S., Elgamal, A., Abdoun, T., Medina, C., Bethapudi, R., and Bennett, V. (2010). "Micromechanical aspects of liquefaction-induced lateral spreading." *International Journal of Geomechanics*, 10(5), 190–201.

Elgamal, A., Dobry, R., and Adalier, K. (1989). "Study of effect of clay layers on liquefaction of sand deposits using small-scale models." *Proceedings of 2nd US-Japan workshop on liquefaction, large ground deformation and their effects on lifelines*, 233–245.

Elgamal, A., Lu, J., and Forcellini, D. (2009). "Mitigation of liquefaction-induced lateral deformation in a sloping stratum: Three-dimensional numerical simulation." *Journal of geotechnical and geoenvironmental engineering*, 135(11), 1672–1682.

Elgamal, A., Yang, Z., and Parra, E. (2002). "Computational modeling of cyclic mobility and post-liquefaction site response." *Soil Dynamics and Earthquake Engineering*, 22(4), 259–271.

Ergun, S. (1952). "Fluid flow through packed columns." *Chem. Eng. Prog.*, 48, 89–94.

Gu, D., Liu, H., Huang, D., Zhang, W., and Gao, X. (2020). "Development of a modeling method and parametric study of seepage-induced erosion in clayey gravel." *International Journal of Geomechanics*, 20(12), 04020219.

Gu, L., Wang, Z., Zhu, W., Jang, B., Ling, X., and Zhang, F. (2021). "Numerical analysis of earth embankments in liquefiable soil and ground improvement mitigation." *Soil Dynamics and Earthquake Engineering*, 146, 106739.

Iai, S., Tobita, T., and Nakahara, T. (2005). "Generalised scaling relations for dynamic centrifuge tests." *Geotechnique*, 55(5), 355–362.

Itasca (2018). "PFC3D (Particle Flow Code in 3 Dimensions), Version 6.0, Minneapolis: ICG.

Iwashita, K. and Oda, M. (1998). "Rolling resistance at contacts in simulation of shear band development by DEM." *Journal of Engineering Mechanics*, 124(3), 285–292.

Kamai, R. and Boulanger, R. (2010). "Characterizing localization processes during liquefaction using inverse analyses of instrumentation arrays." *Meso-scale shear physics in earthquake and landslide mechanics*, 219–238.

Kamai, R. and Boulanger, R. (2013). "Simulations of a centrifuge test with lateral spreading and void redistribution effects." *Journal of geotechnical and geoenvironmental engineering*, 139(8), 1250–1261.

Kokusho, T. (1999). "Water film in liquefied sand and its effect on lateral spread." *Journal of Geotechnical and Geoenvironmental Engineering*, 125(10), 817–826.

Kramer, S. (1996). *Geotechnical Earthquake Engineering*. Prentice Hall, Upper Saddle River, New Jersey.

Liu, H. and Qiao, T. (1984). "Liquefaction potential of saturated sand deposits underlying foundation of structure." *Proceedings of the 8th World Conference on Earthquake Engineering*, 21–28.

Lu, J., Kamatchi, P., and Elgamal, A. (2019). “Using stone columns to mitigate lateral deformation in uniform and stratified liquefiable soil strata.” *International Journal of Geomechanics*, 19(5), 04019026.

Madabhushi, S., Haigh, S., and Madabhushi, G. (2018). “LEAP-GWU-2015: Centrifuge and numerical modelling of slope liquefaction at the University of Cambridge.” *Soil Dynamics and Earthquake Engineering*, 113, 671–681.

Malvick, E., Kutter, B., Boulanger, R., and Kulasingam, R. (2006). “Shear localization due to liquefaction-induced void redistribution in a layered infinite slope.” *Journal of geotechnical and geoenvironmental engineering*, 132(10), 1293–1303.

Markauskas, D., Kruggel-Emden, H., and Scherer, V. (2018). “Numerical analysis of wet plastic particle separation using a coupled DEM-SPH method.” *Powder Technology*, 325, 218–227.

Markauskas, D., Kruggel-Emden, H., Sivanesapillai, R., and Steeb, H. (2017). “Comparative study on mesh-based and mesh-less coupled CFD-DEM methods to model particle-laden flow.” *Powder Technology*, 305, 78–88.

Monaghan, J. (1992). “Smoothed particle hydrodynamics.” *Annual Review of Astronomy and Astrophysics*, 30(1), 543–574.

Monaghan, J. (2000). “SPH without a tensile instability.” *Journal of Computational Physics*, 159(2), 290–311.

Morris, J., Fox, P., and Zhu, Y. (1997). “Modeling low Reynolds number incompressible flows using SPH.” *Journal of Computational Physics*, 136(1), 214–226.

Oda, M., Konishi, J., and Nemat-Nasser, S. (1982). "Experimental micromechanical evaluation of strength of granular materials: effects of particle rolling." *Mechanics of Materials*, 1(4), 269–283.

Olson, S. and Stark, T. (2003). "Yield strength ratio and liquefaction analysis of slopes and embankments." *Journal of Geotechnical and Geoenvironmental Engineering*, 129(8), 727–737.

Radjaï, F. and Dubois, F. (2011). *Discrete-Element Modeling of Granular Materials*. Wiley-Iste.

Sizkow, S. and El Shamy, U. (2021a). "A comparison between coupled SPH-DEM and LBM-DEM approaches for soil liquefaction." *IFCEE*, 53–60.

Sizkow, S. and El Shamy, U. (2021b). "Discrete element method simulations of the seismic response of flexible retaining walls." *Journal of Geotechnical and Geoenvironmental Engineering*, 147(2), 04020157.

Sizkow, S. and El Shamy, U. (2021c). "SPH-DEM simulations of saturated granular soils liquefaction incorporating particles of irregular shape." *Computers and Geotechnics*, 134, 104060.

Soga, K., Alonso, E., Yerro, A., Kumar, K., and Bandara, S. (2016). "Trends in large-deformation analysis of landslide mass movements with particular emphasis on the material point method." *Géotechnique*, 66(3), 248–273.

Sun, X., Sakai, M., and Yamada, Y. (2013). "Three-dimensional simulation of a solid–liquid flow by the DEM–SPH method." *Journal of Computational Physics*, 248, 147–176.

Taboada-Urtuzuastegui, V., Martinez-Ramirez, G., and Abdoun, T. (2002). "Centrifuge modeling of seismic behavior of a slope in liquefiable soil." *Soil Dynamics and Earthquake Engineering*, 22(9-12), 1043–1049.

Thornton, C. (2000). "Numerical simulations of deviatoric shear deformation of granular media." *Géotechnique*, 50(1), 43–53.

Wakai, A. and Ugai, K. (2004). "A simple constitutive model for the seismic analysis of slopes and its applications." *Soils and Foundations*, 44(4), 83–97.

Wu, K., Yang, D., and Wright, N. (2016). "A coupled SPH-DEM model for fluid-structure interaction problems with free-surface flow and structural failure." *Computers & Structures*, 177, 141–161.

Zamani, N. and El Shamy, U. (2011). "Analysis of wave propagation in dry granular soils using DEM simulations." *Acta Geotechnica*, 6(3), 167.

Zhang, W., Zheng, H., Jiang, F., Wang, Z., and Gao, Y. (2019). "Stability analysis of soil slope based on a water-soil-coupled and parallelized smoothed particle hydrodynamics model." *Computers and Geotechnics*, 108, 212–225.

Zhu, Y., Fox, P., and Morris, J. (1999). "A pore-scale numerical model for flow through porous media." *International Journal for Numerical and Analytical Methods in Geomechanics*, 23(9), 881–904.

Zou, Y., Chen, C., and Zhang, L. (2020). "Simulating progression of internal erosion in gap-graded sandy gravels using coupled cfd-dem." *International Journal of Geomechanics*, 20(1), 04019135.

List of Figures

List of Tables

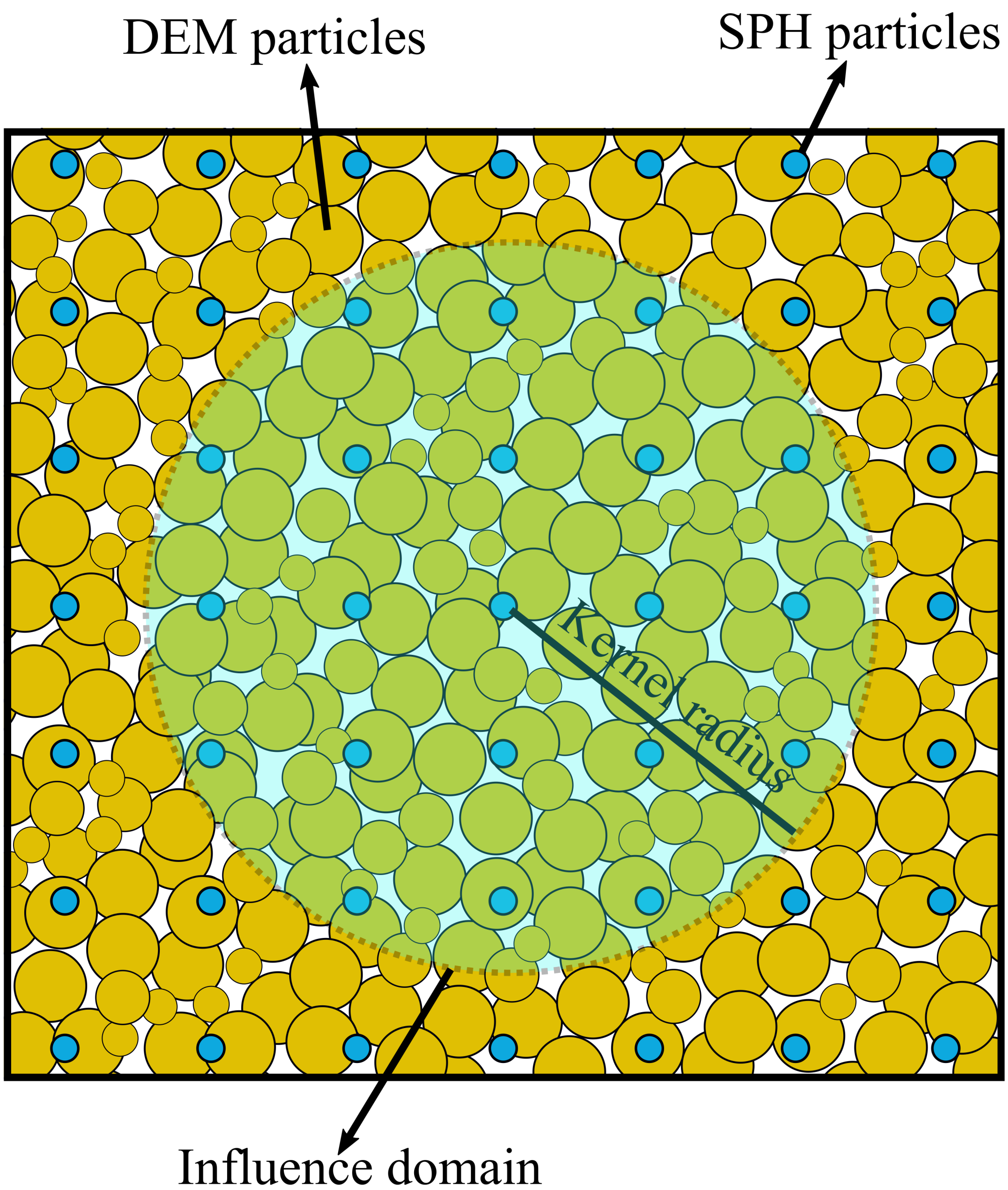

Figure 1: A schematic view of the SPH-DEM model

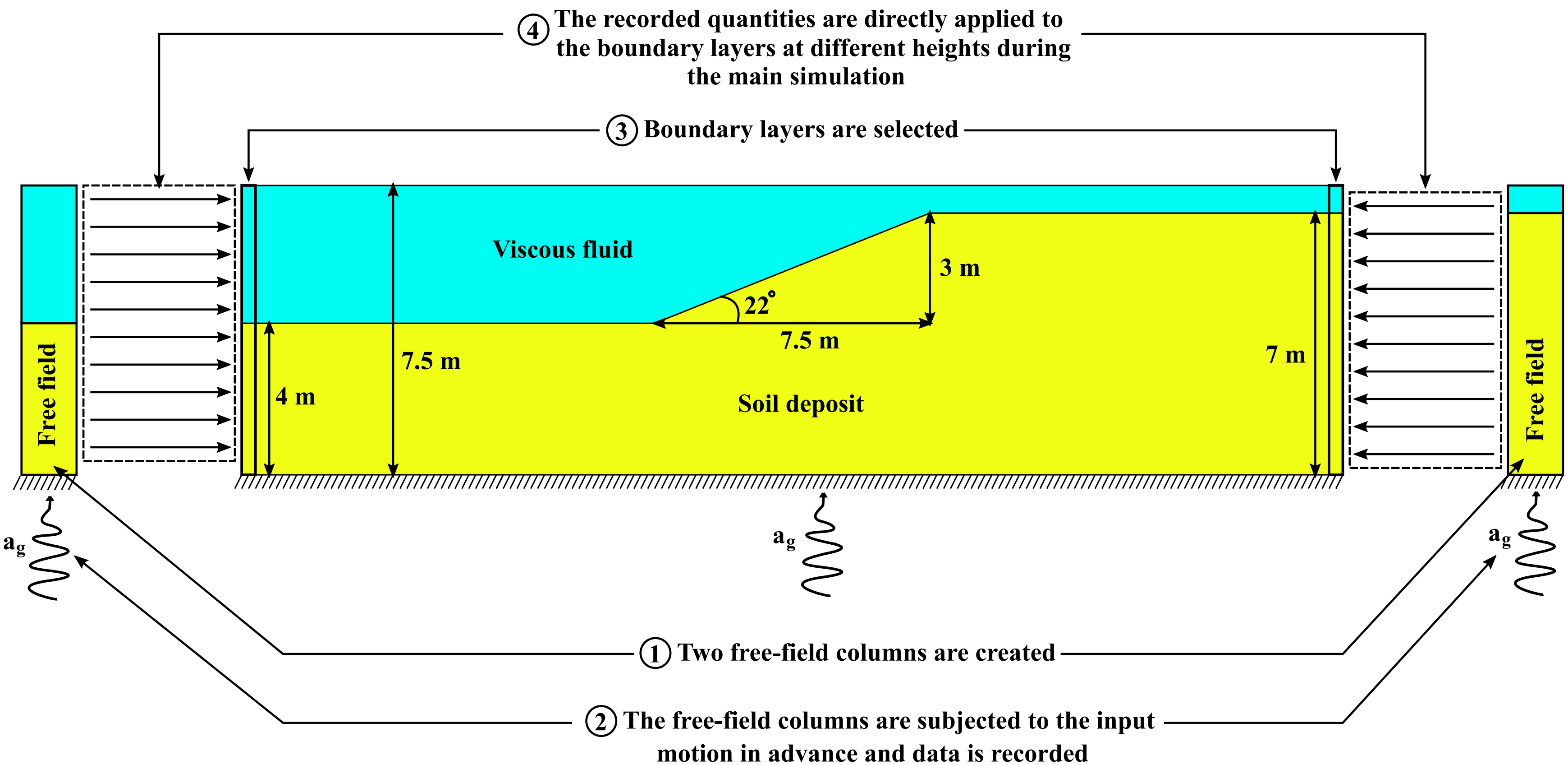

Figure 2: Schematic configuration of the submerged slope

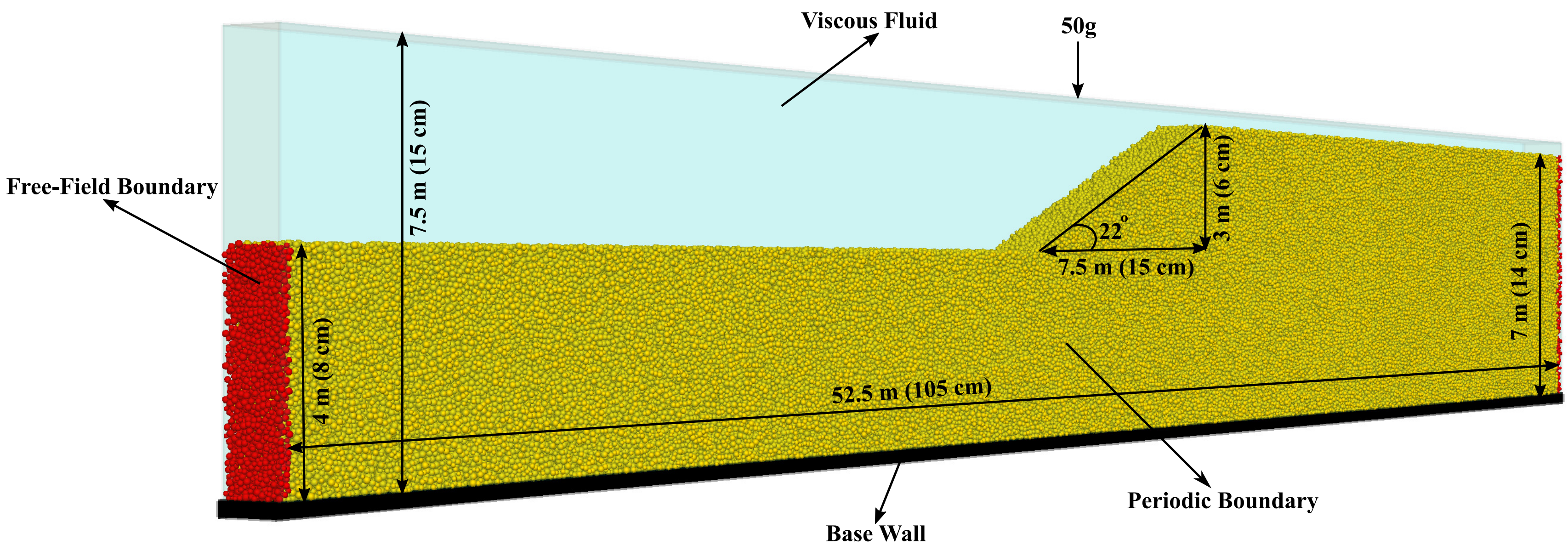

Figure 3: 3D view of the modeled submerged slope

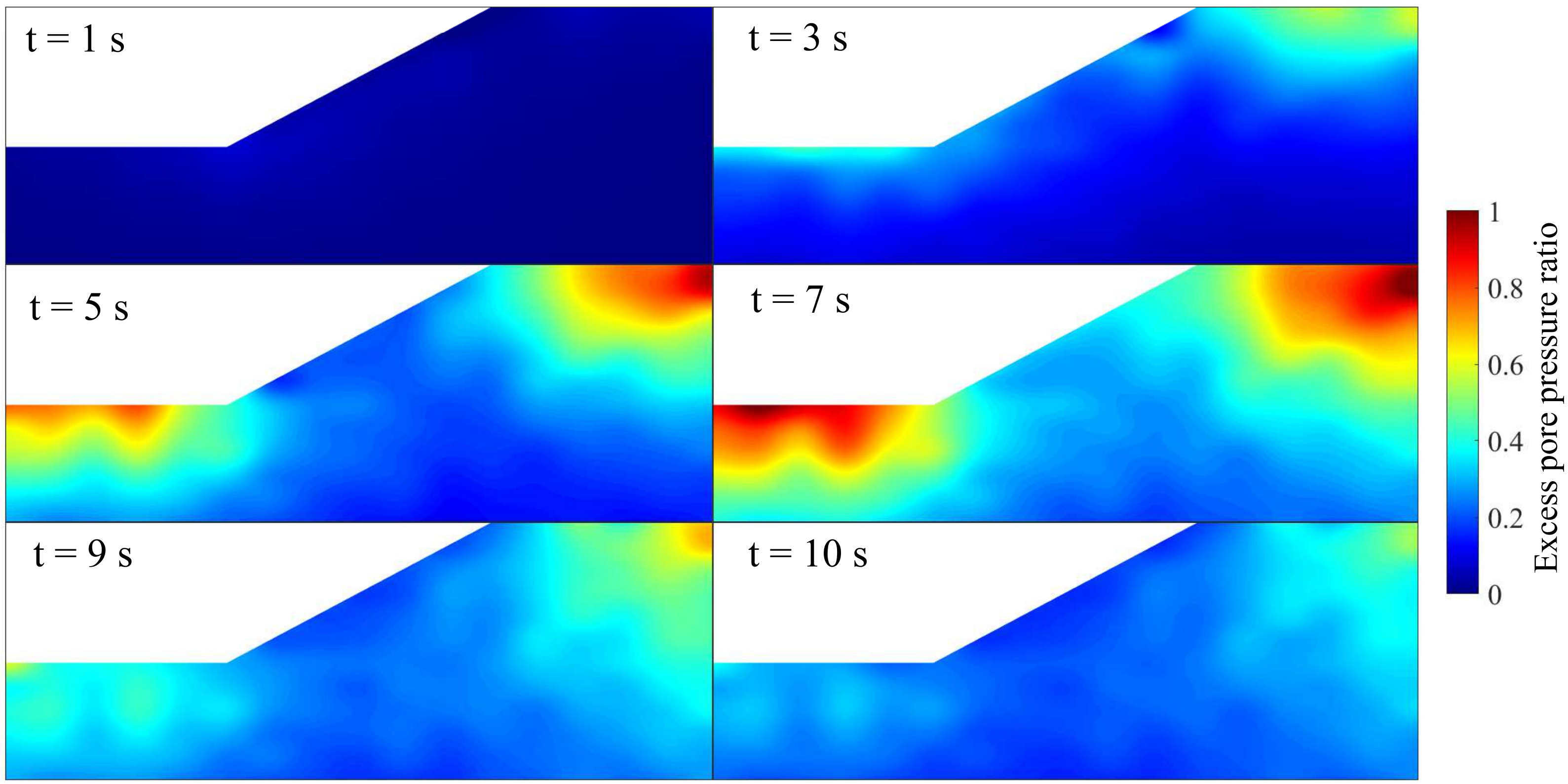

Figure 4: Contours of pore pressure ratio at different time instants (0.1g-3 Hz)

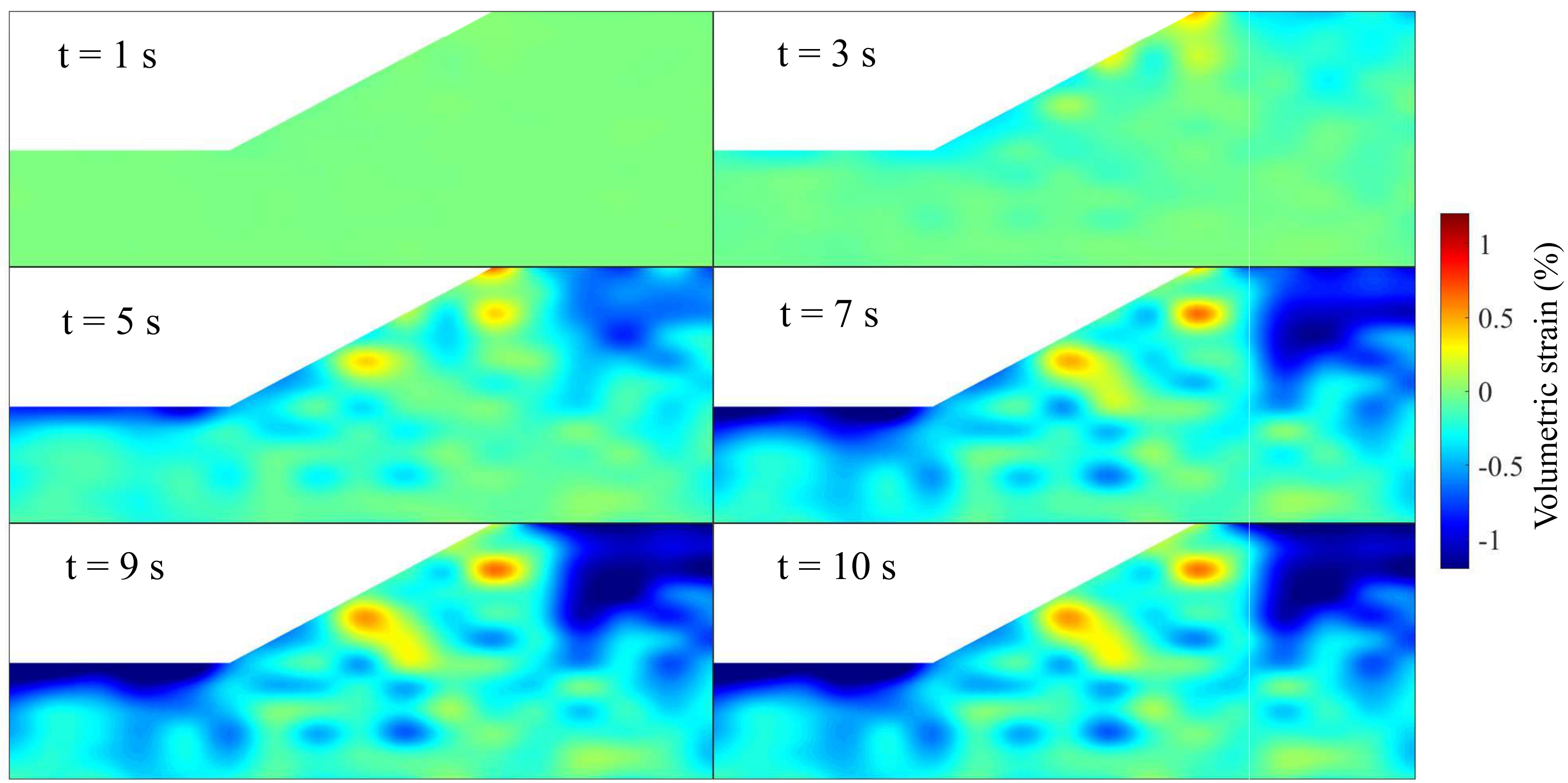

Figure 5: Contours of volumetric strain at different time instants (0.1g-3 Hz)

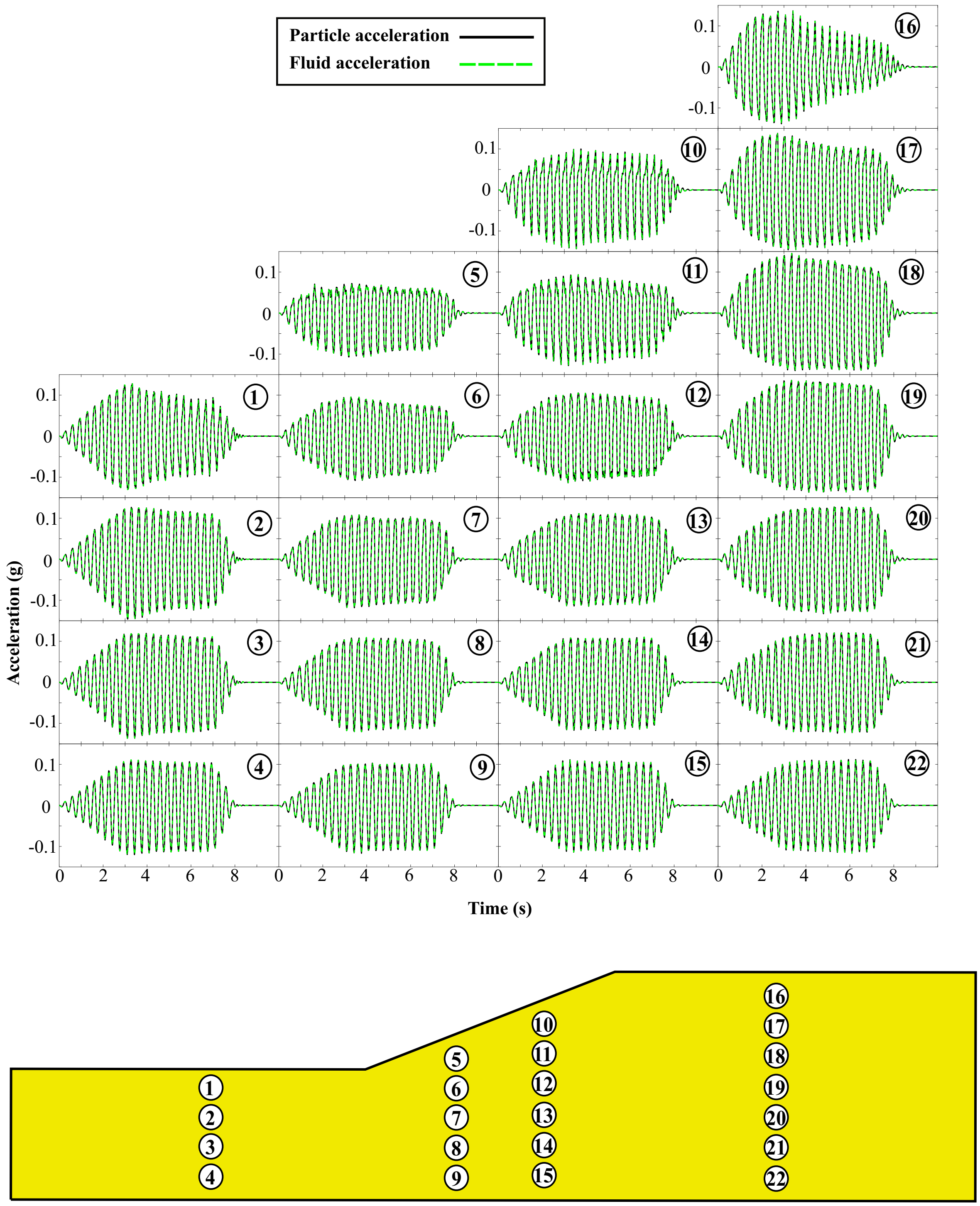

Figure 6: Time histories of average particle acceleration at different locations (0.1g-3 Hz)

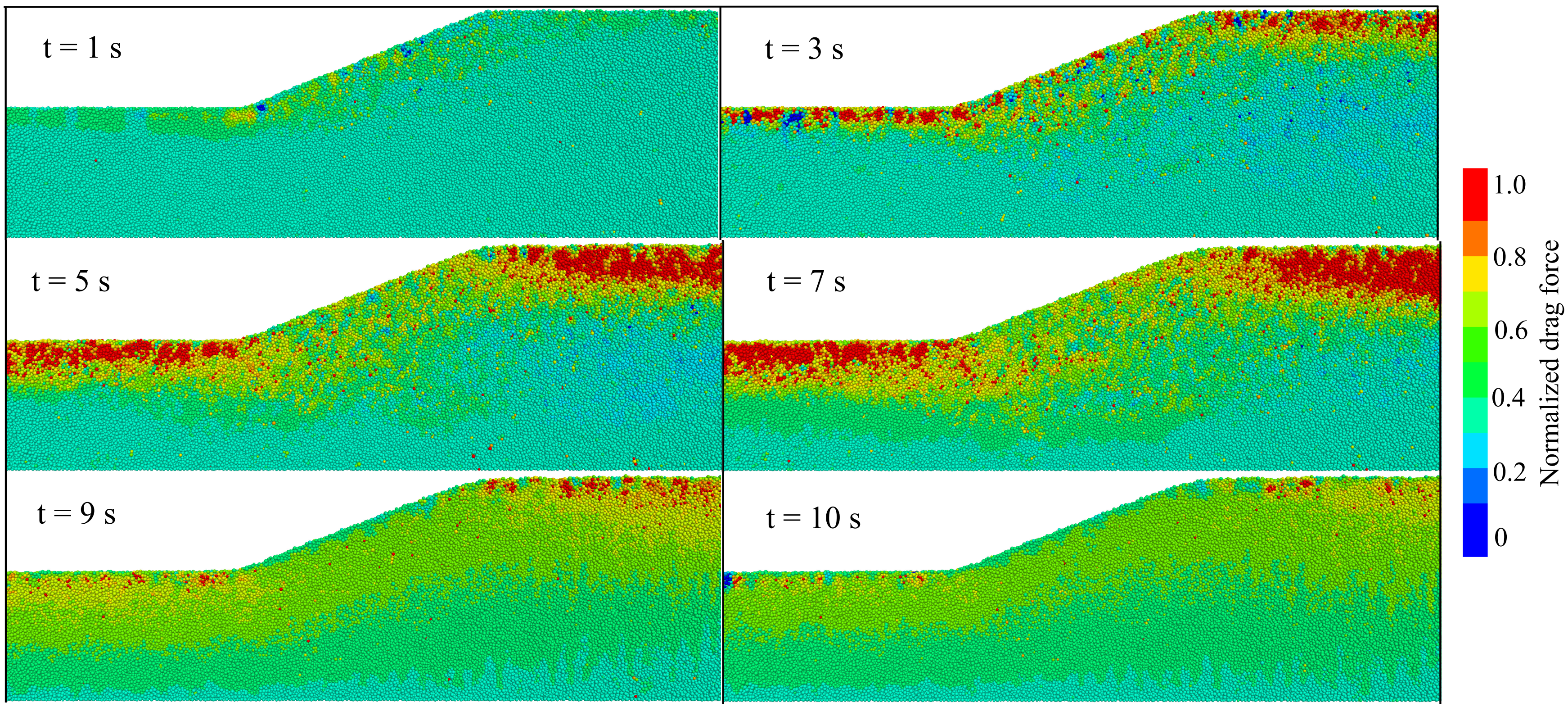

Figure 7: Contours of normalized drag force at different time instants (0.1g-3 Hz)

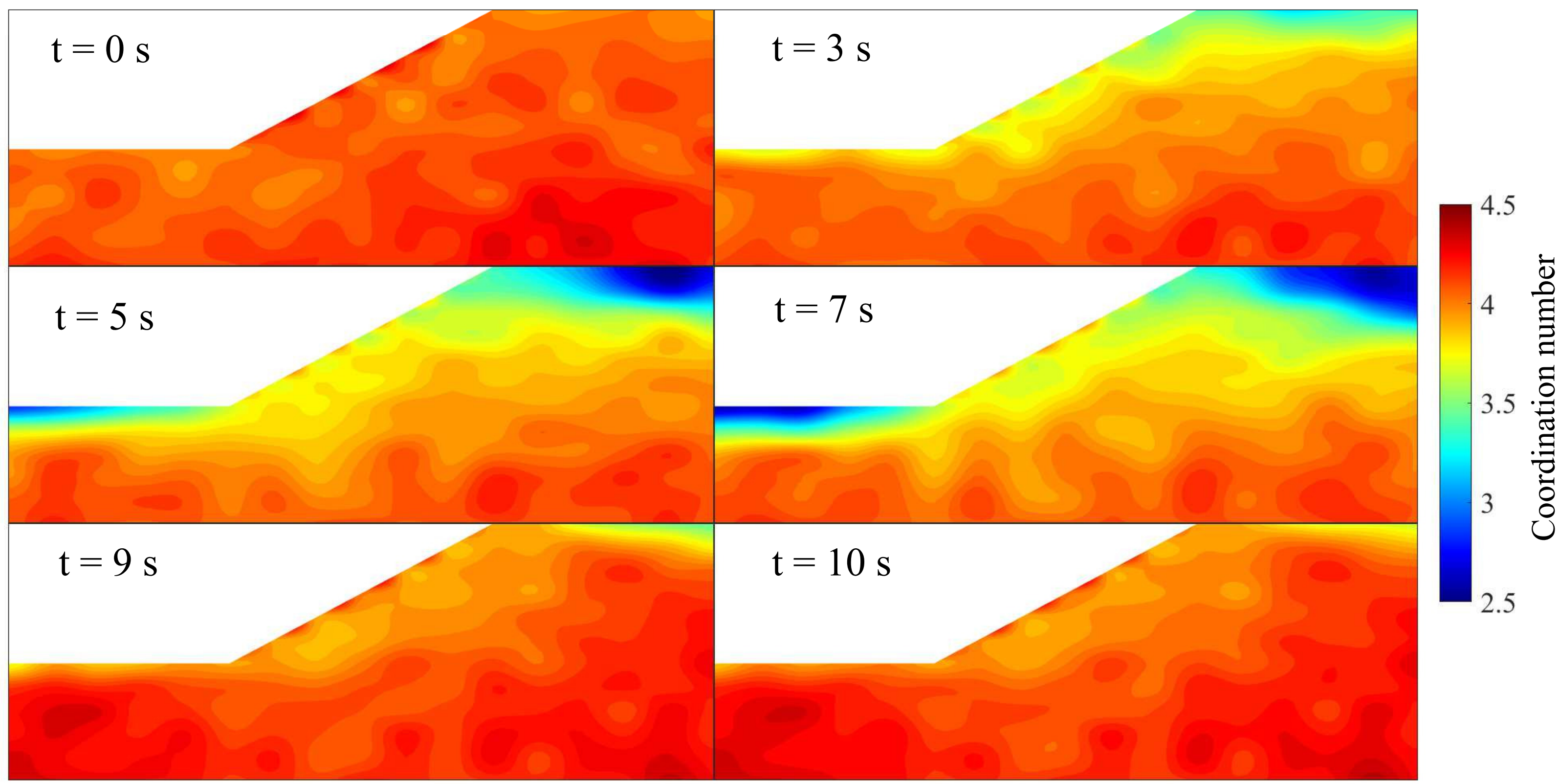

Figure 8: Contours of coordination number at different time instants (0.1g-3 Hz)

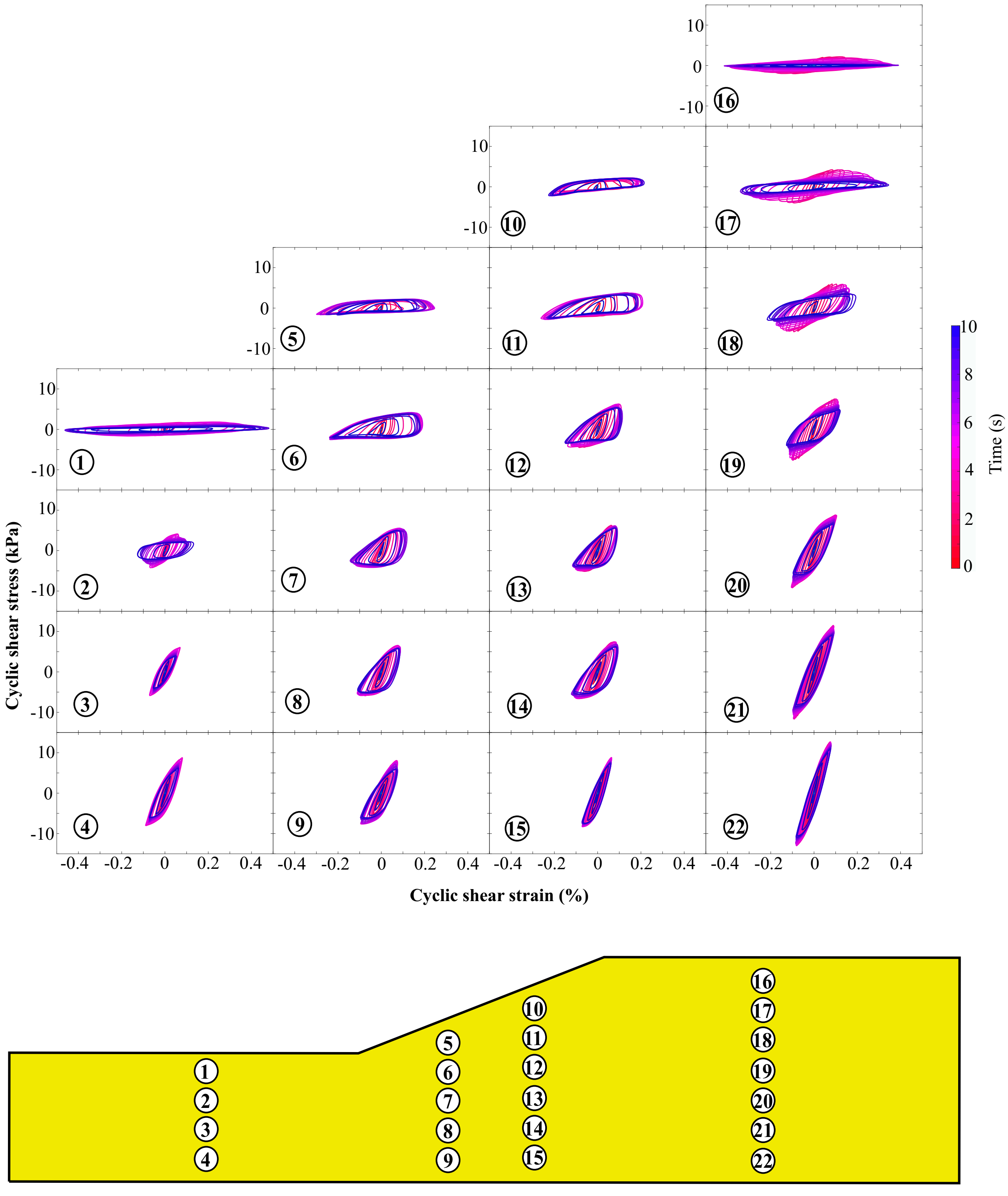

Figure 9: Cyclic shear stress-strain loops at different locations (0.1g-3 Hz)

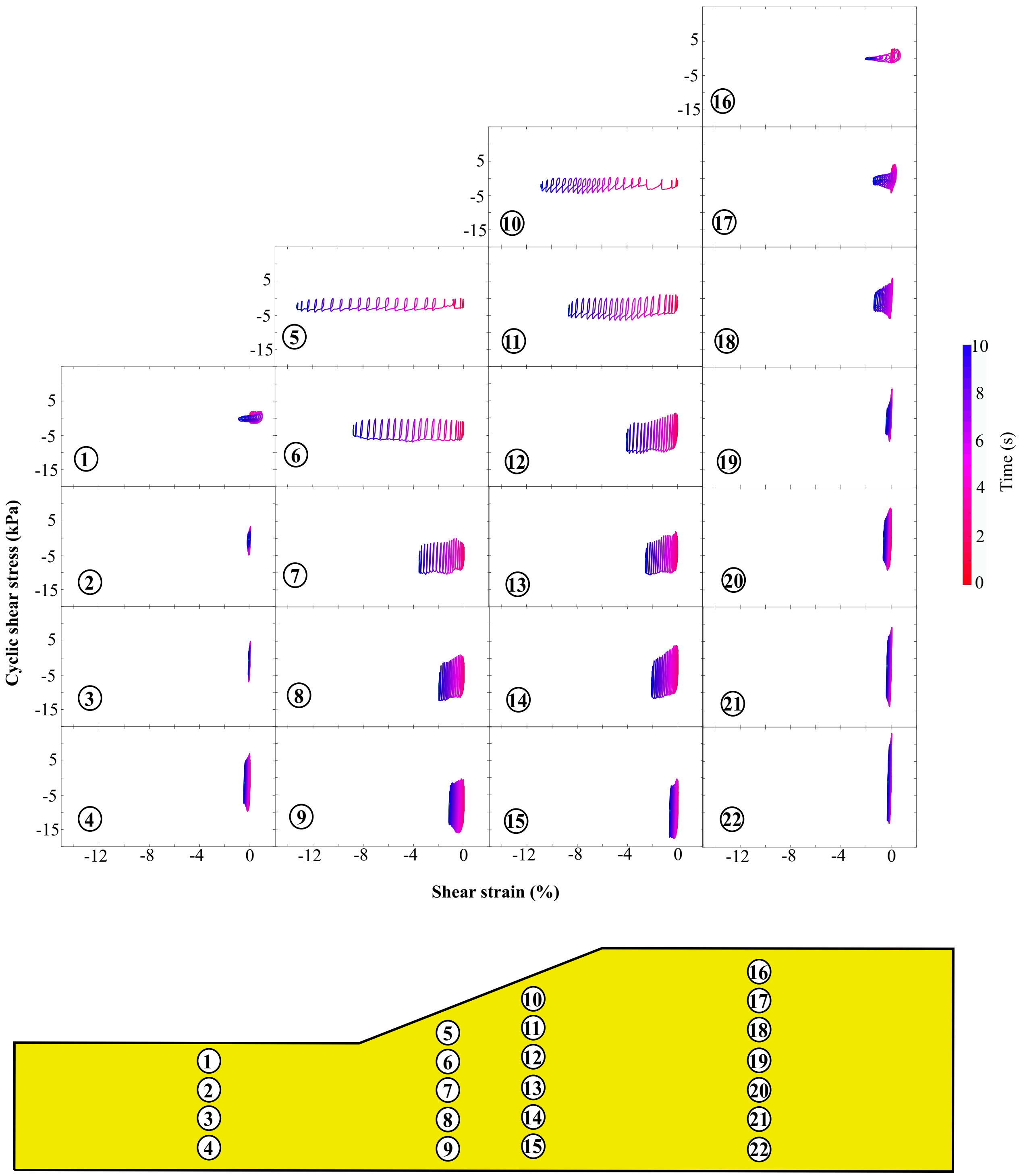

Figure 10: Plots of cyclic shear stress versus total shear strain at different locations (0.1g-3 Hz)

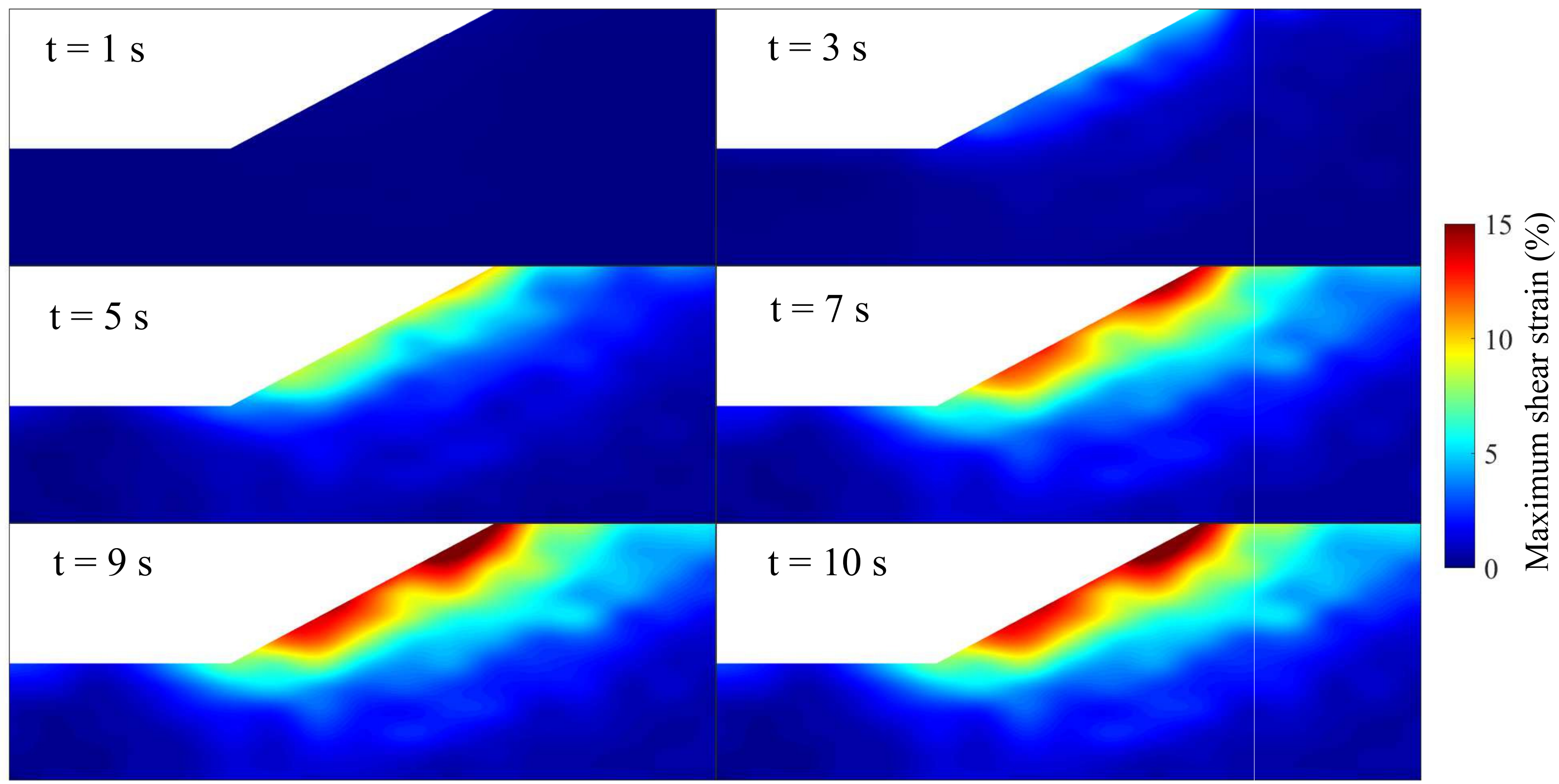

Figure 11: Contours of maximum shear strain at different time instants (0.1g-3 Hz)

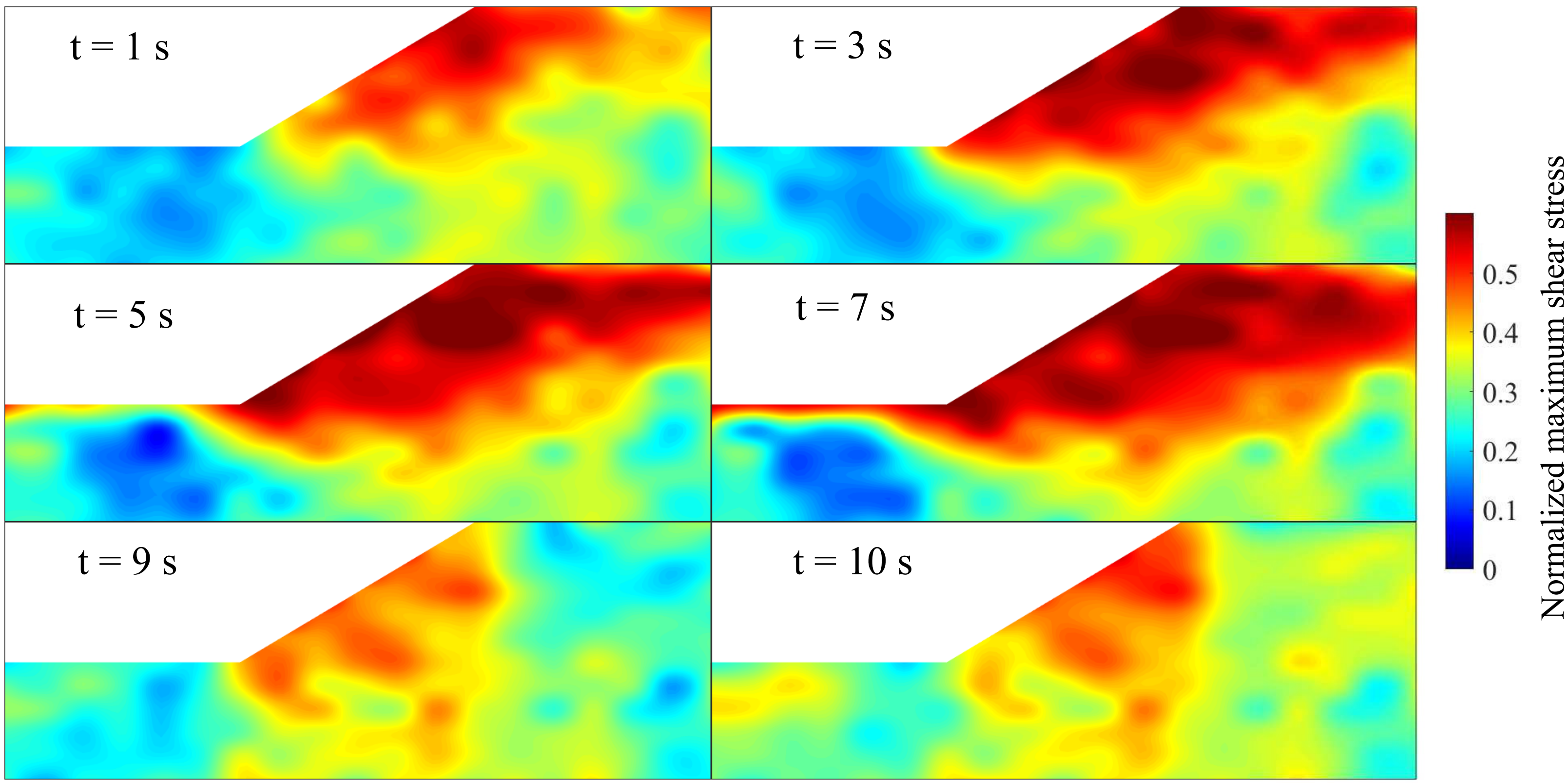

Figure 12: Contours of normalized maximum shear stress at different time instants (0.1g-3 Hz)

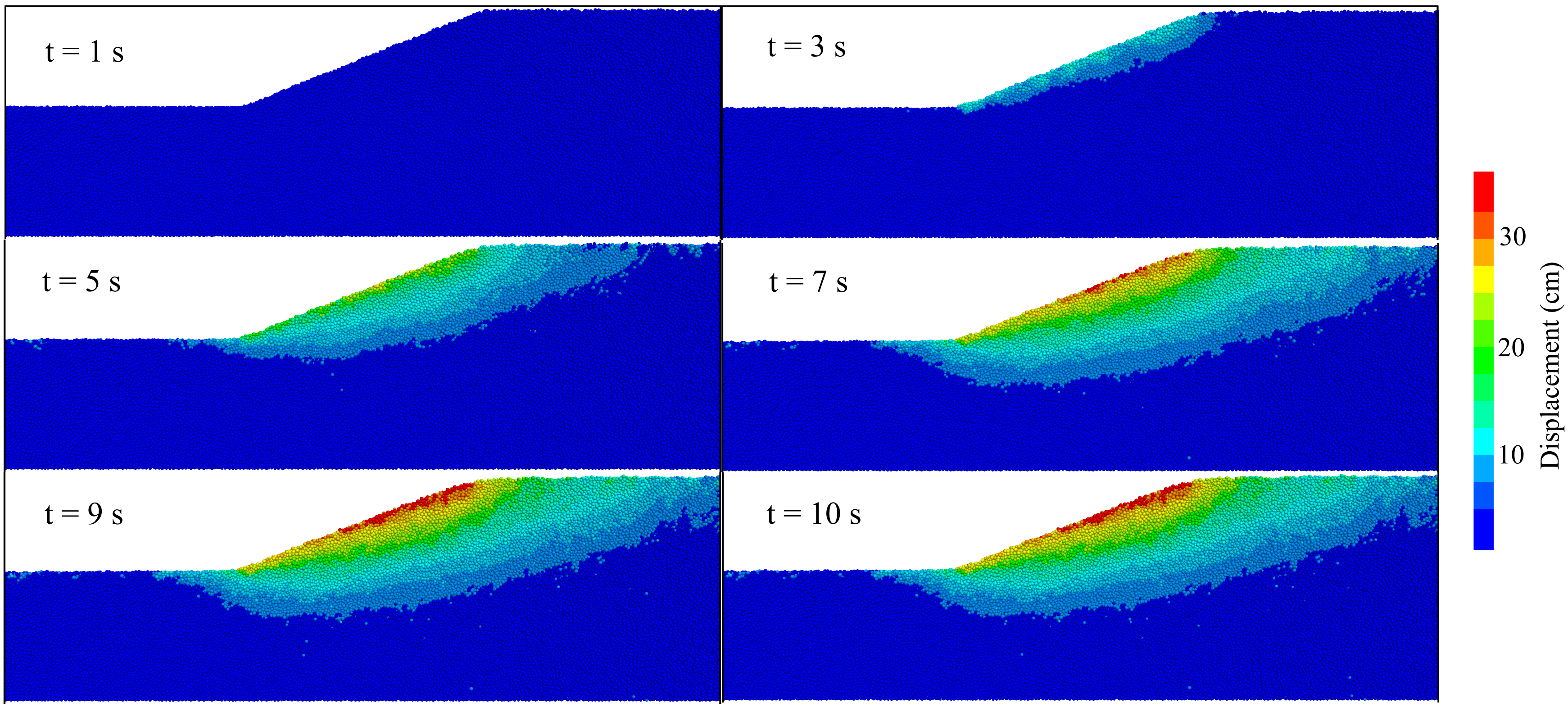

Figure 13: Contours of particle displacement at different time instants (0.1g-3 Hz)

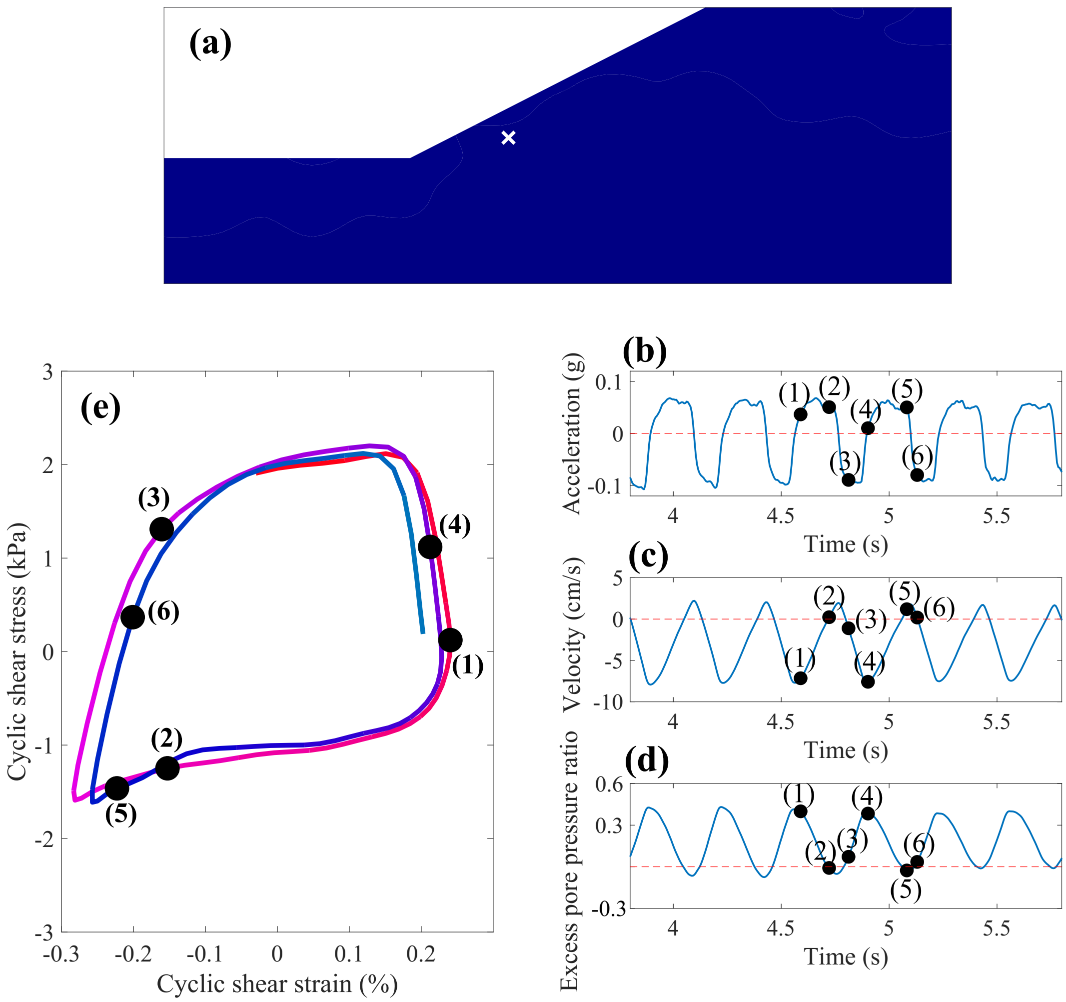

Figure 14: a) Location of the measurement point, b) acceleration time history at the measurement point, c) velocity time history at the measurement point, d) time history of excess pore pressure ratio at the measurement point and e) cyclic shear stress-strain loops at the measurement point (0.1g-3 Hz)

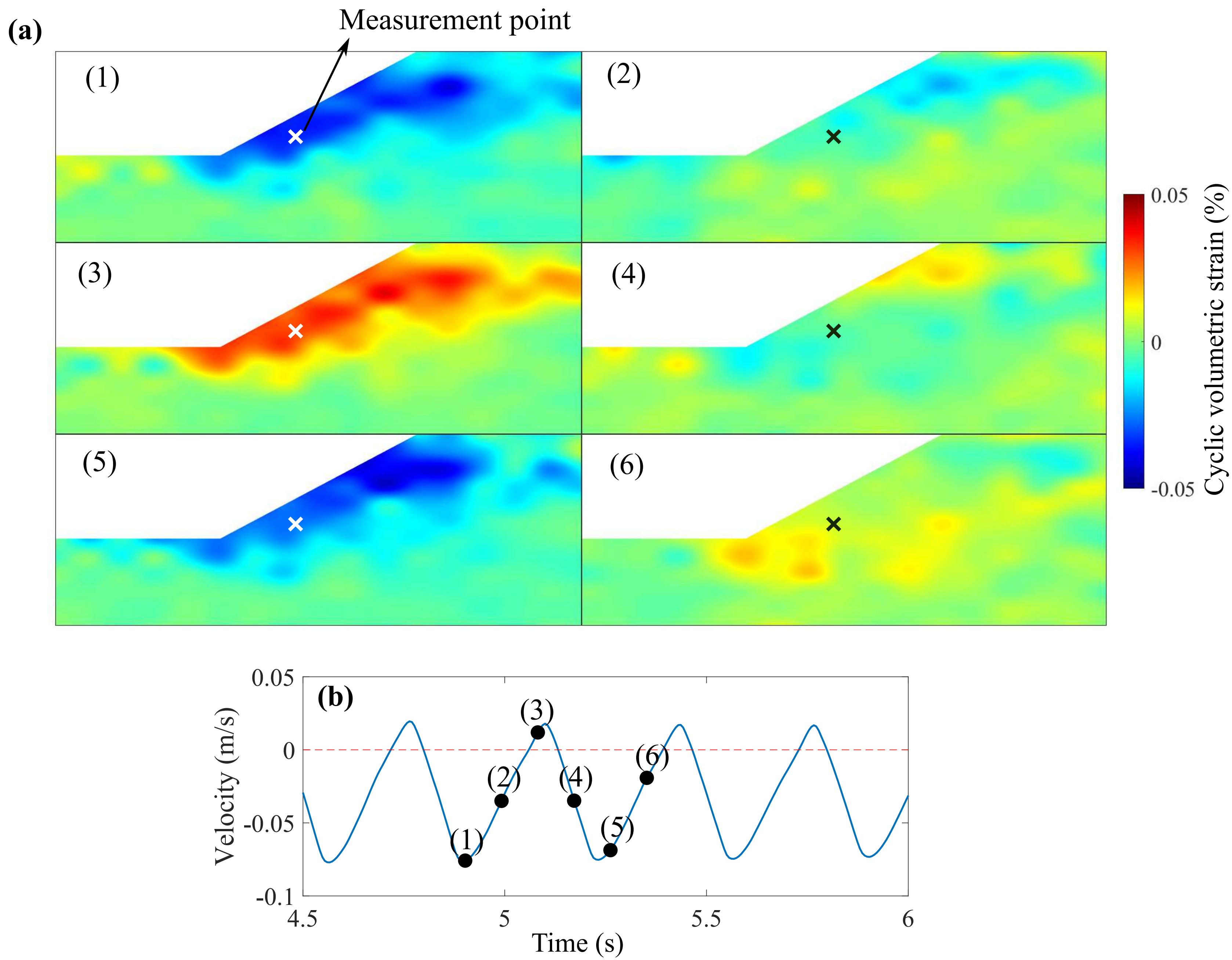

Figure 15: a) Contours of cyclic volumetric strain at the selected time instants and b) velocity time history at the measurement point (0.1g-3 Hz)

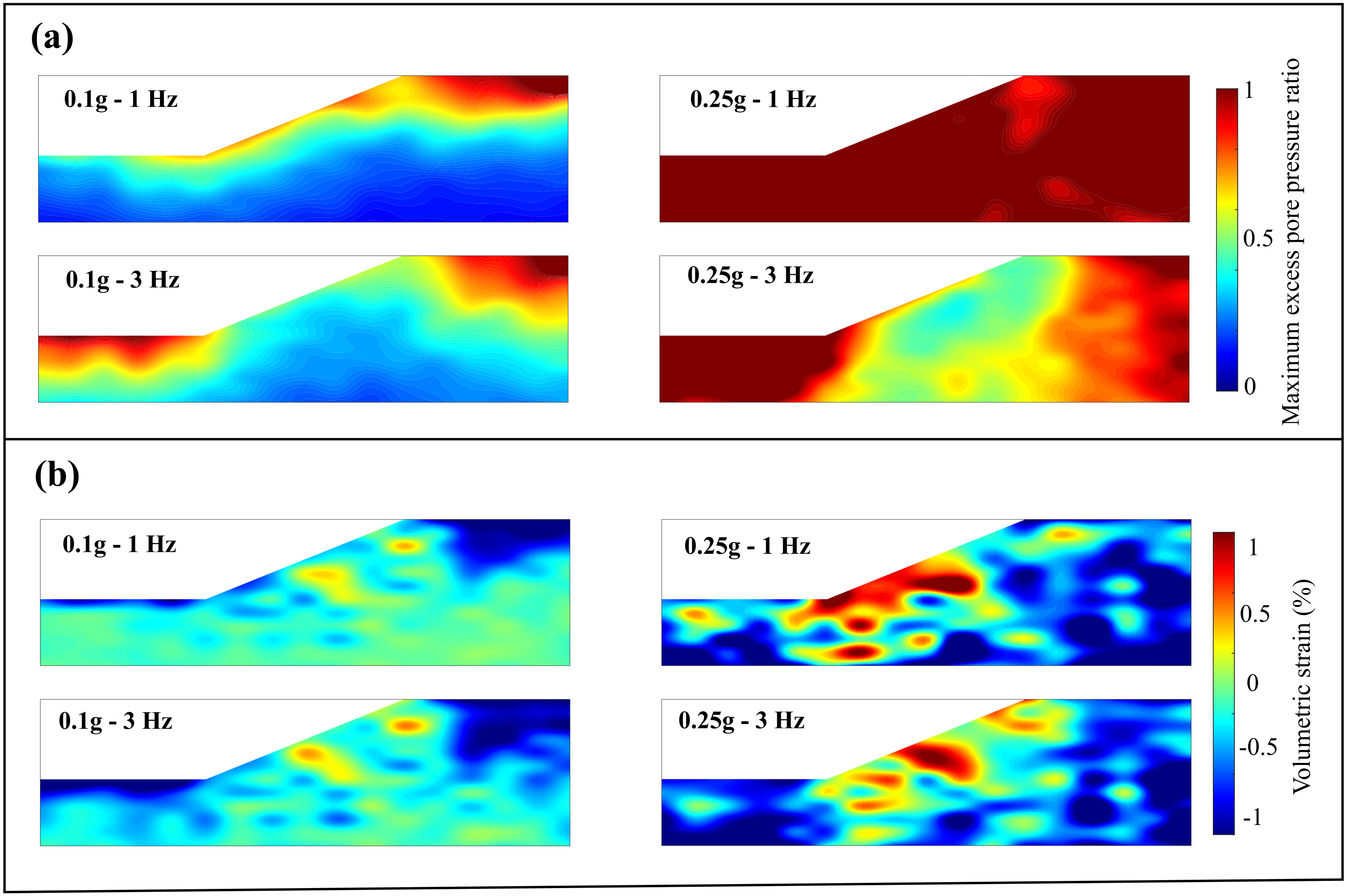

Figure 16: a) Contours of maximum excess pore pressure ratio and b) contours of total volumetric strain for different input motions

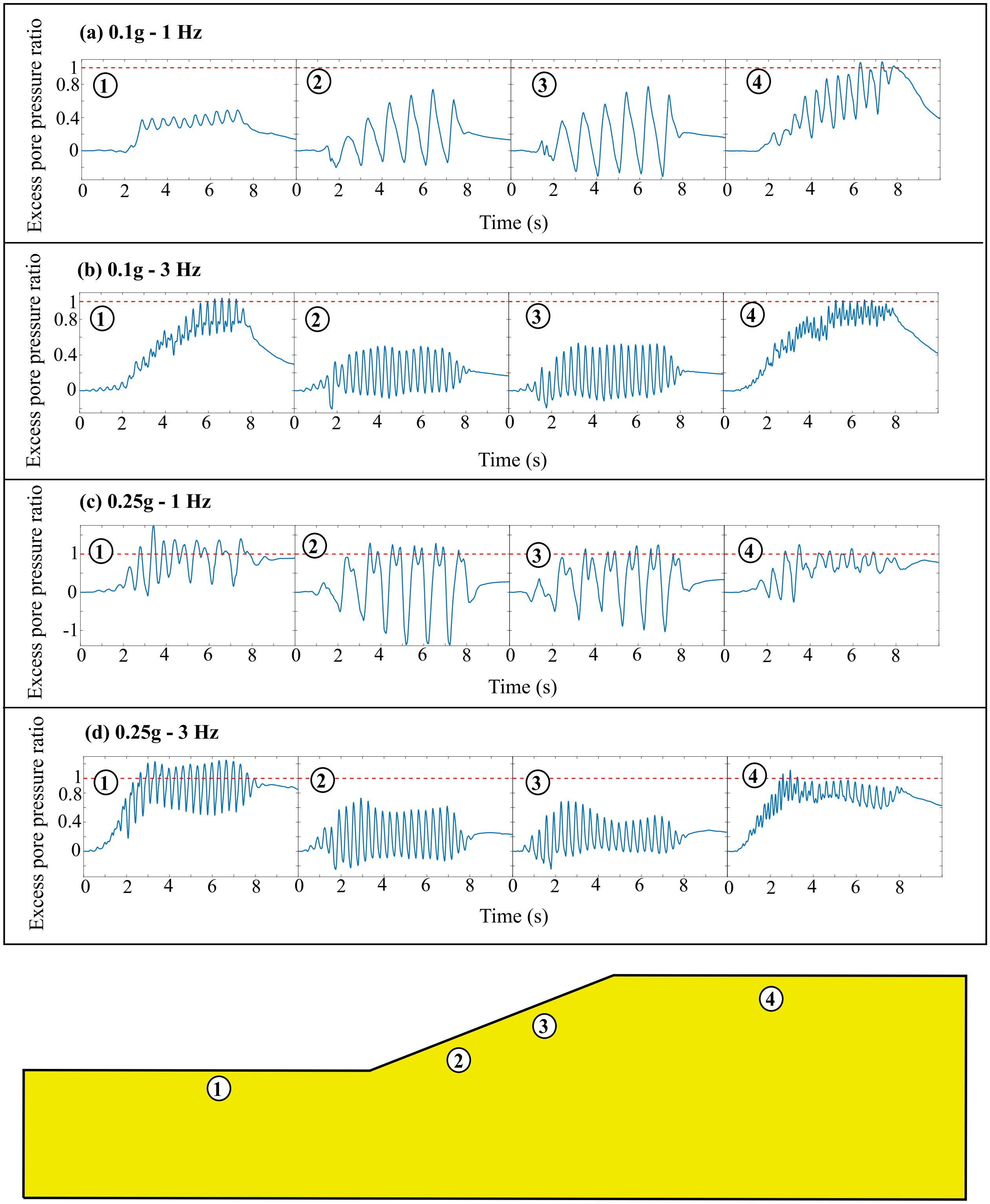

Figure 17: Time histories of excess pore pressure ratio near the ground surface for the input motions of a) 0.1g-1 Hz, b) 0.1g-3 Hz, c) 0.25g-1 Hz and d) 0.25g-3 Hz

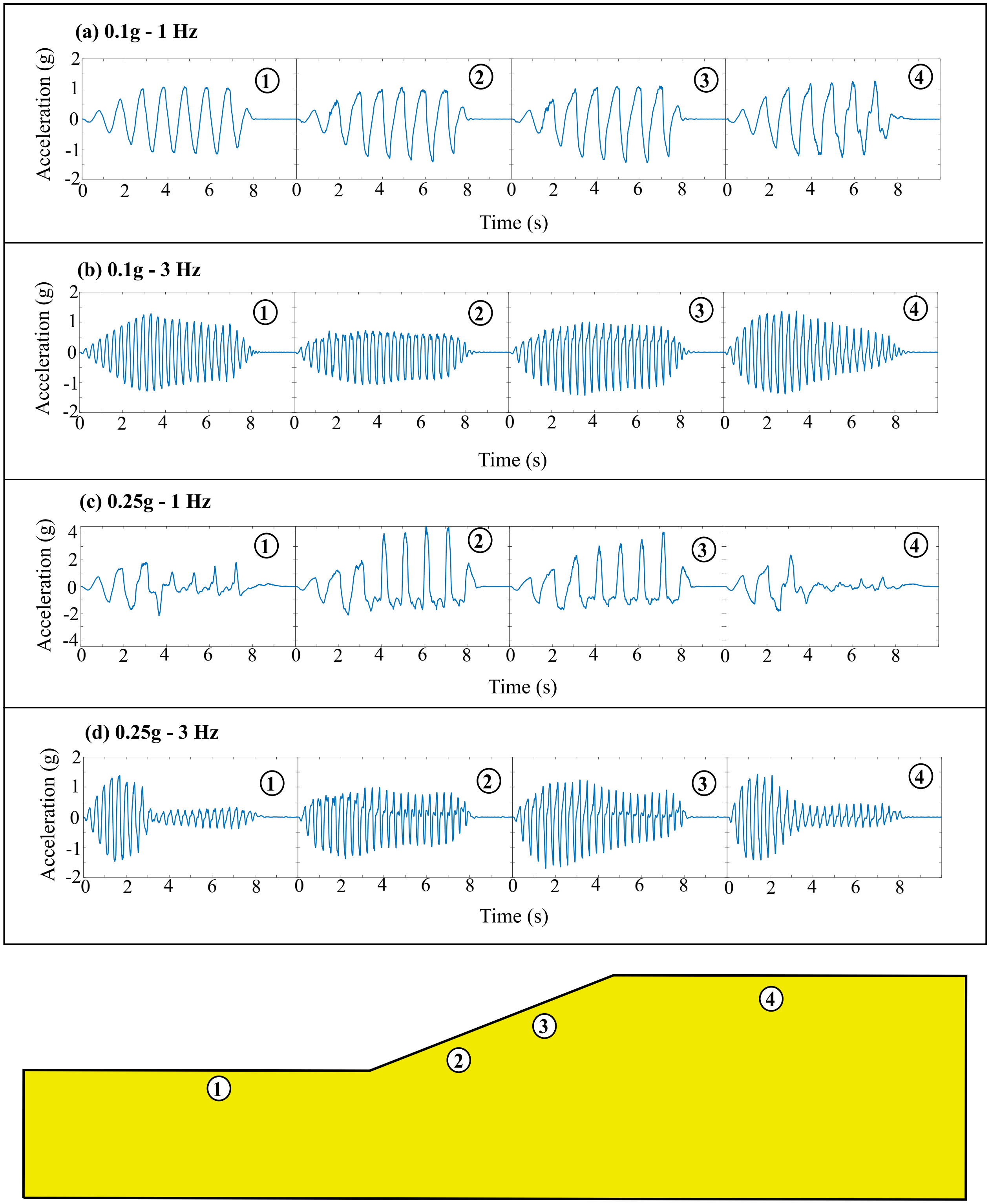

Figure 18: Time histories of average particle acceleration near the ground surface for the input motions of a) 0.1g-1 Hz, b) 0.1g-3 Hz, c) 0.25g-1 Hz and d) 0.25g-3 Hz

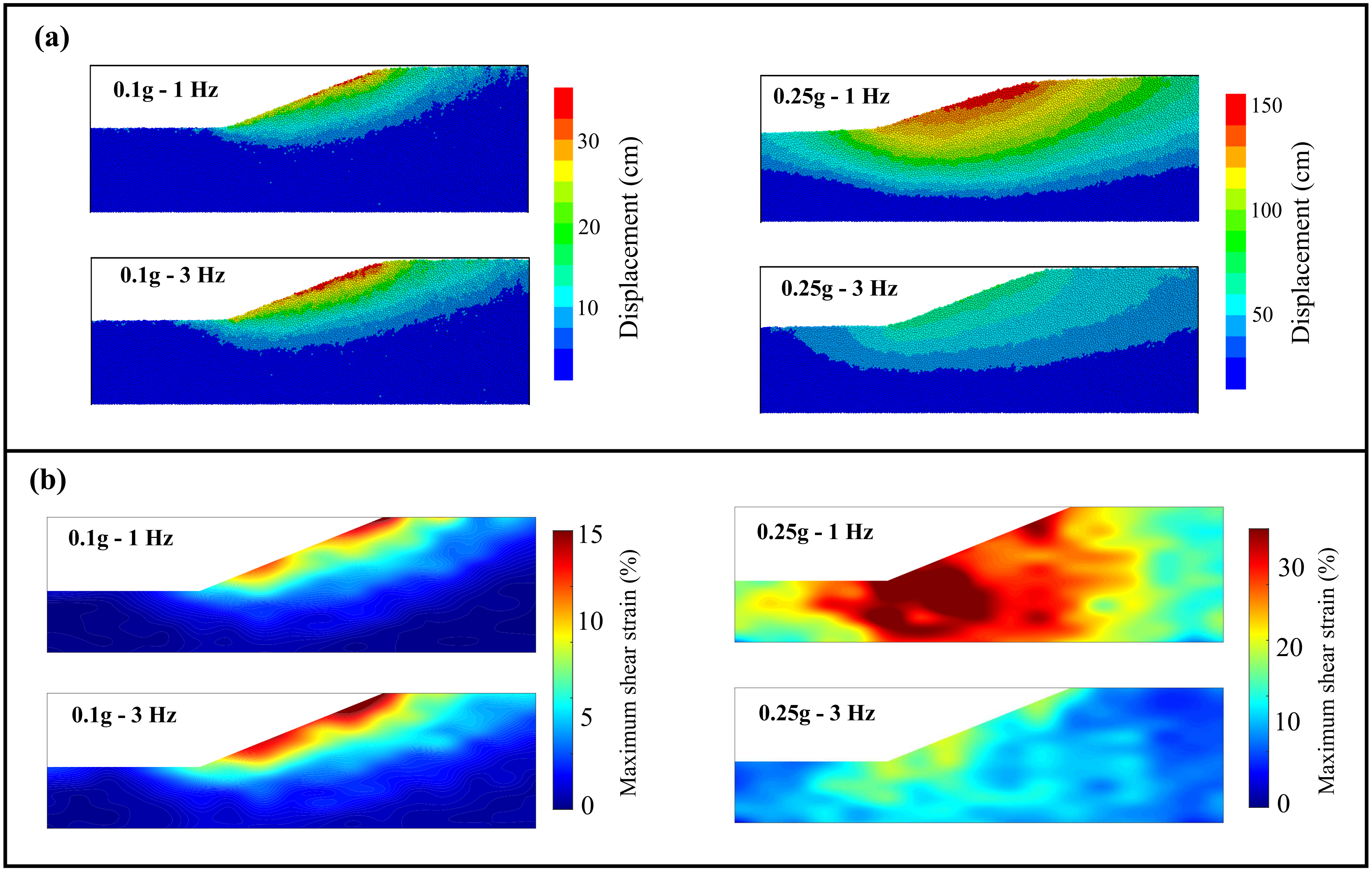

Figure 19: a) Contours of total particle displacement and b) contours of maximum shear strain for different input motions

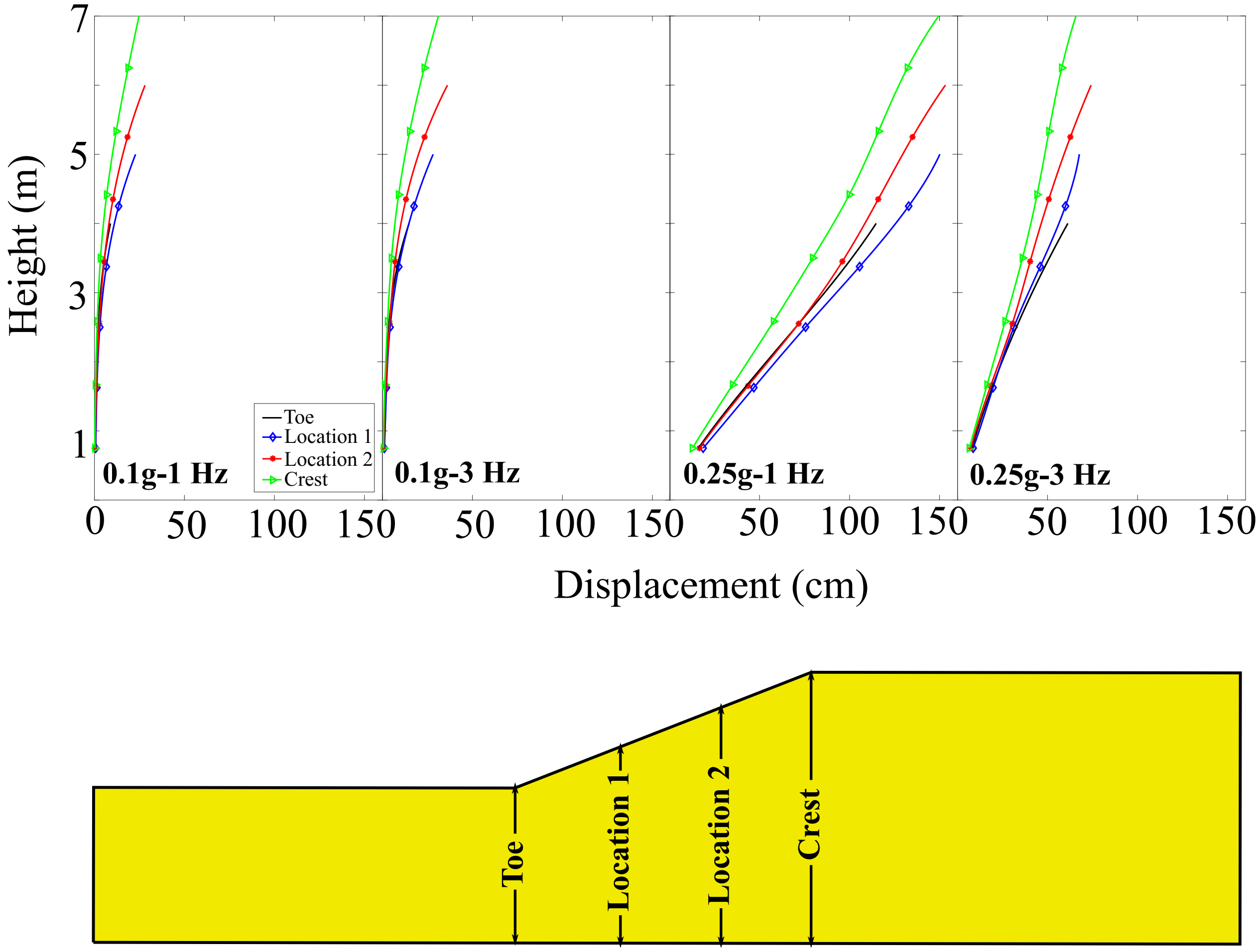

Figure 20: Lateral displacement profiles at the measurement locations for different input motions

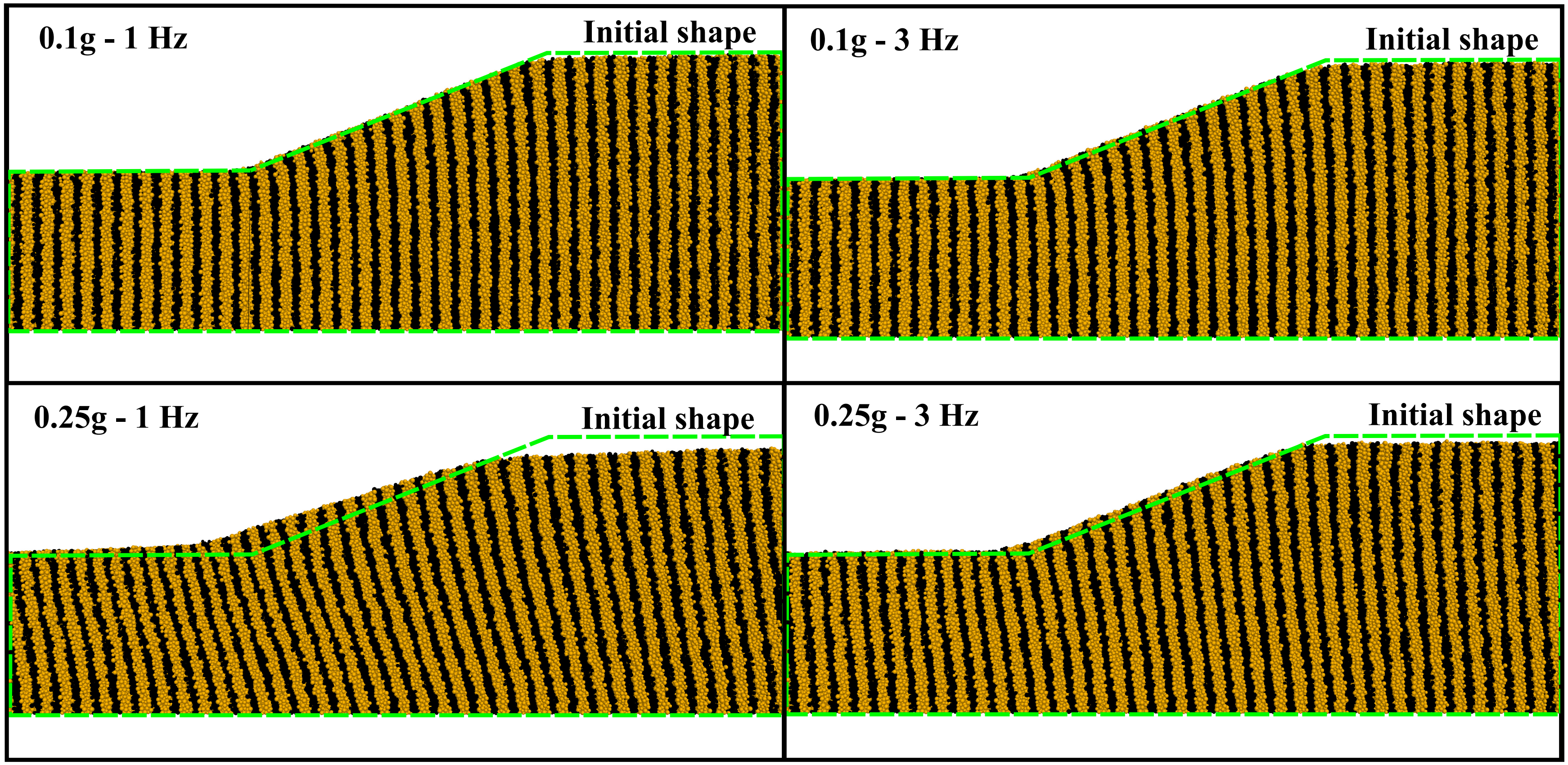

Figure 21: Deformed shapes of the slope at the end of different input motions

Table 1: Simulations details in model units

Soil deposit	
Particle size	1.5 mm to 2.5 mm
Normal stiffness	5.0×10^5 N/m
Shear stiffness	5.0×10^5 N/m
Normal critical damping ratio	0.1
Shear critical damping ratio	0.0
Friction coefficient	0.5
Rolling friction coefficient	0.2
Density	2650 kg/m^3
Number of particles	350000
Viscous Fluid	
Initial spacing	4 mm
Kernel radius	6 mm
Dynamic viscosity	1.0 Pa.s
Density	1000 kg/m^3
Computation parameters	
g-level	50
Time step for DEM	6×10^{-7} s
Time step for SPH	6×10^{-6} s

Table 2: Properties of the soil deposit in prototype units

Unit weight (kN/m^3)	19.0
Porosity	0.43
Fundamental frequency (crest-toe) (Hz)	4.1-7.2
Shear wave velocity (m/s)	114
Low strain shear modulus (MPa)	25.2

Table 3: Free-field amplification factors obtained from DEM simulations and analytical expression

Input frequency (Hz)	Shear modulus (MPa)	Amplification factor (DEM)	Amplification factor (analytical)
3	25.1	2.6	2.47
4	23.6	11.2	12.1
5	25.1	3.2	2.75
6	25.2	1.7	1.46